Dissecting biophysical properties of parvalbumin neurons in the primary visual cortex ensheathed by PNNs

Tarjei Svanes Madland

Thesis

for the Degree of Master in Bioscience

Main field

in neuroscience

60 credits

Program for Cell biology, Physiology and Neuroscience

Department of Biosciences

Faculty of Mathematics and Natural Sciences

UNIVERSITY OF OSLO

2020

Acknowledgements

Abstract

Perineuronal nets (PNNs) are specialized structures of extracellular matrix that are aggregated into mesh-like structures, preferentially ensheathing parvalbumin-expressing (PV^+) interneurons. PV^+ neurons fire action potentials at high frequencies and innervating the cell somata of excitatory neurons, they provide strong inhibitory control of neural networks. Moreover, evidence suggests that they are important regulators of critical period plasticity as well as synchronizing neural activity in the adult brain. It is, however, still unknown how PNNs influence the electrophysiology of these PV^+ neurons. Previous studies have found varying results on the effects of removing PNNs, including increased membrane capacitance and decreased firing rate. However, most of these experiments were performed in young mice in which the PNNs may not be fully developed. Using acute brain slices of the primary visual cortex from adult (>P100) animals of the AcanKO mouse line, I opted to clarify the effects of PNNs on electrophysiology. The AcanKO mice are deficient of aggrecan, a core protein in PNNs, specifically in the CNS, and never develop PNNs. Whole-cell patch-clamp recordings of acute slices show that mice deficient of PNNs from birth have significantly increased membrane capacitance, although there are no differences in action potential frequencies or excitatory input to the PV^+ interneurons. Although the full functions of PNNs remain elusive, this study has found that PNNs decrease the membrane capacitance of PV^+ interneurons. The results also suggest that there might be compensatory mechanisms in mice deficient of PNNs from birth. Furthermore, this study also proposes methodological comparisons of PNN removal for example by chABC or Cre-lox inactivation of critical PNN components.

Table of content

1 Introduction

1.1 Neurophysiology

1.1.1 Passive electrical properties

Neurons are at the core of all the brain´s functions, and the human brain is estimated to consist of about 85 billion neurons in addition to glial cells (Herculano-Houzel, 2014). The main difference between neurons and other cell types is their ability to receive and transmit electrical signals over longer distances, by creating rapid changes in their electrical potential. Neurons have small cell bodies compared to their total size, with branched dendrites and an axon extending from their soma (Kandel et al., 2012b). Like all eukaryotic cells, neurons have a selectively permeable lipid membrane with a conductive intracellular solution. The cable-like structure of axons and dendrites with an insulated conductor allows them to passively transmit electrical signals. Their ability to passively transmit electricity is dependent on the passive electrical properties of the neuron; resting membrane potential (RMP), capacitance, membrane resistance, the time constant and rheobase, that will all be discussed here.

Embedded in the neuronal cell membrane are a variety of ion channels and neurotransmitter receptors. As a consequence of having ion channels, ionic pumps and an impermeable membrane, there is a difference in the ionic composition of the intra- and extracellular medium (Kandel et al., 2012b). The differences in ionic concentration give rise to chemical gradients, in which each ion wants to diffuse towards the lower concentration. In addition to the chemical concentration gradient, there is also an electrical gradient over the cell membrane. The ionic composition of the intracellular space is slightly more negative than the extracellular space due to electrogenic ion pumps, and consequently, there is also an electrical gradient. Ions are affected both by the chemical and the electrical gradient, in a combined electrochemical gradient. Each ion species is affected differently by this gradient, resulting in individual equilibrium potentials for each ion species. The equilibrium potential, E, for a specific ion species can be calculated by the **Nernst equation** (equation 1) and is given as the potential when the electrical gradient precisely counterbalances the chemical gradient of the ion (Molleman, 2003). The equilibrium potentials for all cellular ions add up to make a total membrane potential (Vm), given by the **Goldman equation** (equation 2). Although varying, the RMP for a typical neuron is generally between -50 mV and -80 mV (Kandel et al., 2012b). The resting potentials are always negative because the extracellular space is, by convention, set as the reference point (Molleman, 2003).

$$E_x = \frac{RT}{zF} \ln \frac{[\text{X}]_0}{[\text{X}]_i}$$

Equation 1: The equilibrium potential (E) is expressed by the Nernst equation where, R is the gas constant, T the temperature (in kelvin), z the valence of the ion, F the Faraday constant and [X]o and [X]i is the concentrations of the ion outside and inside of the cell (Kandel et al., 2012a).

$$V_m = \frac{RT}{F} \ln \frac{P_K[K^+]_o + P_{Na}[Na^+]_o + P_{Cl}[Cl^-]_i}{P_K[K^+]_i + P_{Na}[Na^+]_i + P_{Cl}[Cl^-]_o}$$

Equation 2: The membrane potential (Vm) is expressed by the Goldman equation, where P is the permeability for each ion (Kandel et al., 2012a). The concentrations for Cl⁻ are flipped, because Cl⁻ is a negative ion

The lipid bilayer effectively creates ionic and electrical insulation between the conductive intracellular and extracellular space, hence being comparable to an electrical capacitor (Kandel et al., 2012a). A capacitor is an electrical component that can store charge. The capacity of the capacitor is dependent on the thickness of the plate, or the distance separating the two media, and the leakiness between the two media. In a neuron, the capacitance is considered to be uniform over the whole cell, measuring a relative constant $0.9\mu F/cm^2$ (Gentet et al., 2000). However, the membrane is not a perfect insulator. With many ion channels, pumps and some leak channels, the bilayer has a finite resistance that varies with the opening and closing of ion channels (**Figure 1.1**). The opening and closing of channels also effectively change the conductivity of the membrane. Functionally, the capacitance of the membrane introduces a delay to all changes in the membrane potential, and together with the membrane leak limits the propagation and the speed of both sub- and supra-threshold currents (Molleman, 2003). The time constant, tau, is dependent on the membrane resistance and capacitance, and describes the exponential temporal decay of cellular currents. Finally, rheobase is defined as the minimum current injection that is sufficient to engage the transition from passive to active conduction by bringing the membrane potential to threshold, and thereby eliciting action potentials.
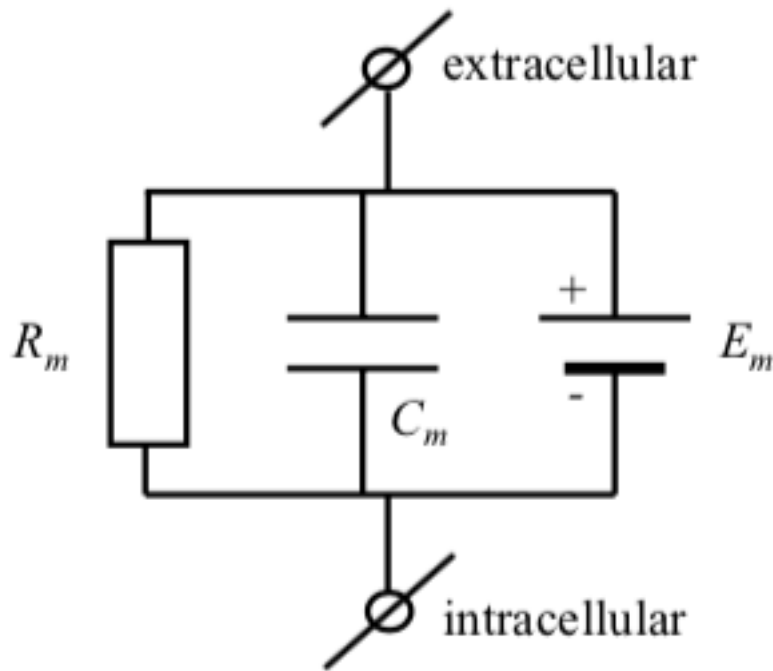
Figure 1.1: *The equivalent circuit of the cell membrane of an intact cell. The membrane capacitance, resistance, and potential are depicted as Cm, Rm and Em respectively. Figure from Molleman (2003).*

1.1.2 Active electrical properties

Although comparable in principle, axons and dendrites have a much lower capacity to passively conduct electricity than regular electrical cables. In order to conduct electrical signals with speed over longer distances and with minimal decay, neurons must engage active propagation of signals in the form of action potentials (APs). Action potentials are mostly generated at the axon initial segment, and only if the sum of the postsynaptic currents from the dendrites and soma are higher than rheobase. At, and above rheobase, the depolarization of the membrane potential is strong enough to reach the threshold for opening voltage-gated ion channels. By opening ion channels, especially the Na^+ and K^+ channels, positive ions flush into the cell giving a much stronger and robust electrical signal in the form of AP (Kandel et al., 2012b). APs are regenerative, and will propagate along the axon without decay. Action potentials are also all or none responses. If, and only if the cell reaches the membrane potential threshold, an action potential will be elicited. Although action potentials are all or none responses, the shape and time scale of an action potential can have subtle differences, depending on the cell type and specific ion channel kinetics. AP features such as threshold, amplitude, half-width and after-hyperpolarizations are commonly measured. Other interesting features to study are the maximum frequency at which a cell can fire, and if the cell adapts to a prolonged stimulus. These active properties can differ quite a lot between different cell types, and can encode different information to the postsynaptic cell through the release of neurotransmitters. For the purpose of this study, only AP frequency, membrane capacitance and spontaneous excitatory postsynaptic currents (sEPSCs) will be discussed.

1.1.3 Capacitance estimation in the whole-cell patch-clamp configuration

As the cellular membrane acts as a leaky capacitor, and the specific membrane capacitance of neurons is considered to be $0.9\mu F/cm^2$ (Gentet et al., 2000), total membrane capacitance is directly proportional to the total membrane surface of the neuron. Because neurons commonly have complex morphology, with an array of branched dendrites and an axon, the total membrane area is not easily attainable through experimental measurements alone. However, estimates of total membrane capacitance through whole-cell patch-clamp experiments can be useful to indicate approximate cell size. Commonly, one of three different patch-clamp procedures are applied to approximate membrane capacitance; a current-clamp step protocol, a voltage-clamp ramp protocol or a voltage-clamp step protocol.

In the current-clamp step estimation, 30 sweeps of a 500 ms hyperpolarization step (**Figure 2.1**) are averaged to eliminate noise. The square step current is injected, and in a typical multi-compartment cell, the resulting membrane potential change is given by a series of exponentials. Each exponential is expressed by **Equation 3**, representing electrical potential equalizations between electrical compartments of the cell. From the exponential with the slowest time constant, equation 3 can be resolved so that the total membrane capacitance can be extracted from the definition of the time constant: $\tau_m = R_m C_m$ (Golowasch et al., 2009) (**Figure 3.2**).

$$V_m(t) = V_{rest} \sum_{i=0}^{\infty} V_i(1 - e^{-\frac{t}{\tau_0}})$$

Equation 3: The resulting membrane potential change (Vm(t)) in a cellular compartment after injecting a square current step. V_{rest} is the resting potential, V_i is the potential at different times, t, in the current step and τ_0 is the slowest time constant. Equation from (Golowasch et al., 2009)

In a typical voltage ramp protocol, a 10mV ramping hyperpolarizing step immediately followed by a 10mV ramping depolarizing step is injected in a cell kept at a baseline resting potential. Recording the resulting currents from the voltage ramps, the capacitive currents, i_c, can be recorded as $2i_c$ at the shift from hyperpolarization to depolarization. Membrane capacitance can then be found from **Equation 4**, where dV_m/dt is the slope of the ramping steps (Golowasch et al., 2009).

$$i_c = \frac{dQ}{dt} = C_m \frac{dV_m}{dt}$$

Equation 4: The capacitive current resulting from the voltage ramp, where dQ is the change in charge, i_c is the capacitive current and dV_m/dt is the slope of the ramping steps. Equation adapted from (Golowasch et al., 2009)

In the voltage-clamp step protocol, membrane capacitance is calculated from the total accumulated charge on the membrane in the capacitive current (Golowasch et al., 2009). By applying 1000 ms voltage steps of about -50mV, the charge and membrane capacitance can be calculated from **Equation 5** and **Equation 6**, where t_p is the step duration and i_c is the capacitive current.

$$Q = C_m \Delta V_m$$

Equation 5: The relationship between charge (Q), membrane capacitance (Cm) and change in membrane potential (ΔVm). Equation from (Golowasch et al., 2009)

$$Q = \int_0^{t_p} I_c dt$$

Equation 6: Calculation of the total charge of the capacitive current after an applied voltage step. Equation from (Golowasch et al., 2009)

The membrane capacitance protocols all assume that the patched neuron is isopotential, consisting of a single, small, spherical compartment – an assumption that is violated by most neurons (Golowasch et al., 2009). In the current-clamp step protocol, this is partly compensated for by yielding more than one exponential as the voltage differences equalize between electrical compartments, and the capacitance and be calculated from the slowest one. The voltage-clamp protocols don´t compensate for multiple compartments, leading to a severe underestimation of estimated *Cm*. The current-clamp protocol is therefore, by far, the most accurate method to estimate total membrane capacitance, and the estimated Cm also seems to be adequately comparable to the actual *Cm* in most cases (Golowasch et al., 2009). The advantage of using voltage-clamp methods, such as the one provided in the Membrane Test function of Clampex (pClamp, Molecular Devices), is that it allows real time estimations of Cm without having to calculate capacitive transients. Although underestimating actual Cm, such real time estimations are useful to monitor relative changes in Cm during recordings, rather than performing post-recording calculations to estimate Cm, as with the current-clamp step protocol.

To accurately calculate the absolute membrane capacitance however, more complex, computational multi-compartmental modeling must be performed. A multi-compartmental model must account for the cellular morphology and use cable modeling to compute how the voltage changes as current passes through all the branches of dendrites and axons. This is far more laborious and complex than estimating total membrane capacitance by using the current-clamp step protocol, and in most cases, the estimated Cm is sufficiently accurate.

1.1.4 Excitatory and inhibitory neurons

There is general discrimination between excitatory neurons, most of which are classified as pyramidal neurons, and inhibitory neurons, conventionally called interneurons. The excitatory pyramidal cells are abundant in cell layers 2 through 6 of cortex (Connors and Gutnick, 1990), and in each layer or brain area, most of the pyramidal cells are also aligned almost in parallel. Although numerous types of excitatory cells are described, the general neurotransmitter used by excitatory cells is glutamate (Bekkers, 2011). In contrast to pyramidal cells, the soma of inhibitory interneurons is usually rounder and flatter with a less defined apical-basal polarization, although interneurons exhibit a plethora of morphologies (Huang and Paul, 2019). Their projections are shorter, non-spiny with GABAergic synapses confined within the same brain area as the cell soma, mostly spreading in a layer-specific manner (Kubota, 2014;

Tremblay et al., 2016). The non-pyramidal interneurons are also prominent in layers 2 through 6, constituting approximately 15-20% of the neocortical neurons (Connors and Gutnick, 1990; Kubota, 2014).

Electrophysiological recordings also seem to imply that there is a correlation between the general morphology and physiology of excitatory pyramidal cells and the GABAergic interneurons, although both groups are heterogeneous. The majority of the pyramidal cells show regular, quite broad, action potentials (spikes) with prolonged repolarization and a complex variety of after-hyperpolarization and after-depolarization. Furthermore, the regular spiking (RS) cells fire at lower frequencies, and show pronounced adaptation to stimuli (Connors and Gutnick, 1990). Conversely, the GABAergic interneurons of the parvalbumin-family generally seem to be fast-spiking (FS) cells with minimal adaptation (Kubota, 2014; Tremblay et al., 2016). Because of more rapid repolarizations and brief, but deep after-hyperpolarizations, FS cells can obtain much higher spiking frequencies than the RS cells with frequencies of several hundred Hz over several hundred ms (Connors and Gutnick, 1990).

1.1.5 Diversity and classification of interneurons

Although the GABAergic parvalbumin-neurons comprise a large group of inhibitory neurons, at least ten different groups of inhibitory neurons are known, most of which originate from non-pyramidal cells (Hu et al., 2014; Kubota, 2014). However, interneurons are a minority compared to the numerous excitatory cells, and because of the huge diversity in distribution, morphology and physiology of these cells, they have been difficult to classify unequivocally (Kawaguchi and Kubota, 1997; Petilla Interneuron Nomenclature et al., 2008). Fortunately, due to advances in research techniques, and a huge effort within the field the last two decades, morphological and molecular markers are emerging as tools for unambiguous classification of GABAergic interneurons (Hu et al., 2014; Tremblay et al., 2016) (**Figure 1.2**). Because interneurons are so heterogeneous, and have been so hard to classify, several classification systems are used in the literature. However, to ensure unequivocal classification, the interneurons must be placed into sub-groups based on clear non-overlapping markers. Three such markers have been found to cover close to 100% of all GABAergic interneurons; parvalbumin (PV), Somatostatin (Sst) and the ionotropic serotonin receptor (5HT3aR) (Lee et al., 2010; Tremblay et al., 2016). The 5HT3aR interneurons are further divided into vasoactive intestinal peptide (VIP) positive and VIP negative 5HT3aR interneurons, including double bouquet and neuroglial cells (Lee et al., 2010). This study will concentrate on the fast-spiking GABAergic interneurons in the primary visual cortex that are also expressing the protein parvalbumin (PV). These are briefly described in the section below (see 1.1.6).

The next step in classification is based on morphology and anatomy, as these features restricts and gives information about possible input and output targets (Kawaguchi and Kubota, 1997). Moreover, physiology and firing pattern are also important for classification, and the interneurons are as heterogeneous here as in the other features. While excitatory pyramidal

cells are usually adapting and fire broad action potentials at with low frequencies, interneurons cover most of the specter of firing patterns, including RS, FS, burst spiking, low threshold spiking and late spiking patterns (Kawaguchi and Kubota, 1997). The firing patterns are not, however, always consistent with the morphological groups, although they are important and valuable parameters of classification. The physiology of the cells is also more sensitive to the experimental setup (temperature, stimulating current etc.) than the other parameters used for classification. In the recent years, genetic approaches, such as single cell RNA sequencing have also been used to give an even more detailed classification, and search for new sub-group markers. While big efforts have been made to classify different groups of interneurons, a fresh study by Scala et al. (2020) has revealed an almost continuous specter of electrophysiology within and between defined cell types, highlighting the difficulty of unequivocal classification.
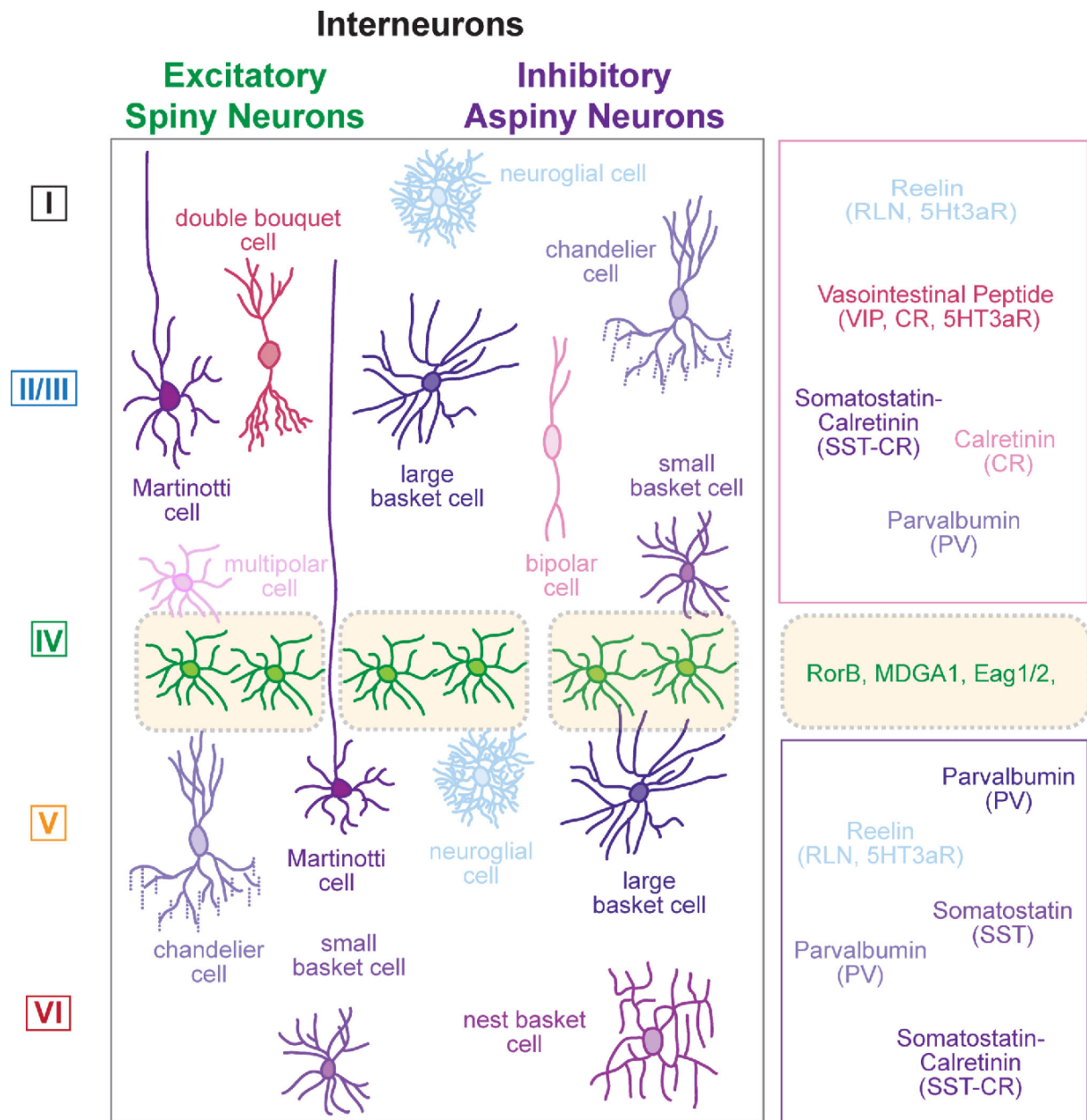
Interneurons

Figure 1.2: Interneuron diversity

Diversity in interneuron morphology and distribution. Most interneurons are of non-pyramidal cell origin and are inhibitory, but the spiny stellate cells in L IV are excitatory interneurons of pyramidal origin. Figure by Lodato and Arlotta (2015).

1.1.6 Parvalbumin-expressing interneurons

Parvalbumin (PV) is a calcium binding protein which is characteristic of a large subgroup of GABAergic interneurons, most of which are fast-spiking. In fact, 40% of GABAergic interneurons are PV[+], including almost all fast-spiking interneurons (Tremblay et al., 2016). The PV^{+} neurons are further divided into two main subgroups; basket cells and chandelier cells. They can be separated mostly on morphology, as the basket cells synapse onto the soma and proximal dendrites of their targets, while chandelier cells are axo-axonic (Kawaguchi and Kubota, 1997; Tremblay et al., 2016). The axonic targets combined with strong inhibition by fast GABAergic release, suggest a particularly powerful inhibitory role for the PV[+] interneurons

(Hu et al., 2014). In the neocortex, basket cells are the most abundant of the two groups, and although both are fast-spiking, basket cells are slightly faster than chandelier cells (Tremblay et al., 2016). Although slightly different, both groups of PV$^+$ interneurons are specialized for speed, efficiency and temporal precision (Tremblay et al., 2016) The ability to sustain fast, non-adapting spiking activity over time is permitted by several molecular and biophysical specializations. Most notably, PV$^+$ cells express high levels of the Kv3, especially the Kv3.1b voltage-gated potassium channels, that allow for quick deactivation and rapid repolarizations (Hartig et al., 1999; Tremblay et al., 2016). Hu and Jonas (2014) also found that PV$^+$ basket cells in the rat hippocampus are dependent on fast sodium channels with an increasing density from the soma to the proximal axon and increasing even further to the distal axon.

In addition to intrinsic cellular specializations, PV$^+$ cells also seem to make use of extracellular components to maintain high frequency spiking. Several studies have shown that approximately 90% of the PV$^+$ GABAergic interneurons in the primary visual cortex are also covered in perineuronal nets, or PNNs for short (Carulli et al., 2010; Celio and Blumcke, 1994; Hartig et al., 1999; Lensjo et al., 2017; Pizzorusso et al., 2002; van 't Spijker and Kwok, 2017). In the auditory brainstem, some of the fastest spiking neurons known can reach spiking frequencies of up to 1000 Hz. These neurons do not develop their super-fast spiking ability until P14, which correlates well with the development of PNNs in the auditory brainstem (Balmer, 2016). Therefore, it has been proposed that the PNNs somehow facilitates the fast spiking in these, and other fast-spiking neurons. The fast-spiking, PV$^+$ interneurons in the primary visual cortex are the subjects of this study.

1.2 Perineuronal nets

Perineuronal nets (PNN) are reticular structures that tightly enwrap the cell body and proximal dendrites of many neurons (Celio and Blumcke, 1994; Wang and Fawcett, 2012) (**Figure 1.3**). They are a type of specialized extracellular matrix (ECM), resembling cartilage, that is unique to the central nervous system (CNS) (Deepa et al., 2006). PNNs were first described by Camillo Golgi in 1898, over a century ago, but it is first in the last 30-40 years that the discovery has received noteworthy attention and research (reviewed by Vitellaro-Zuccarello et al., 1998).
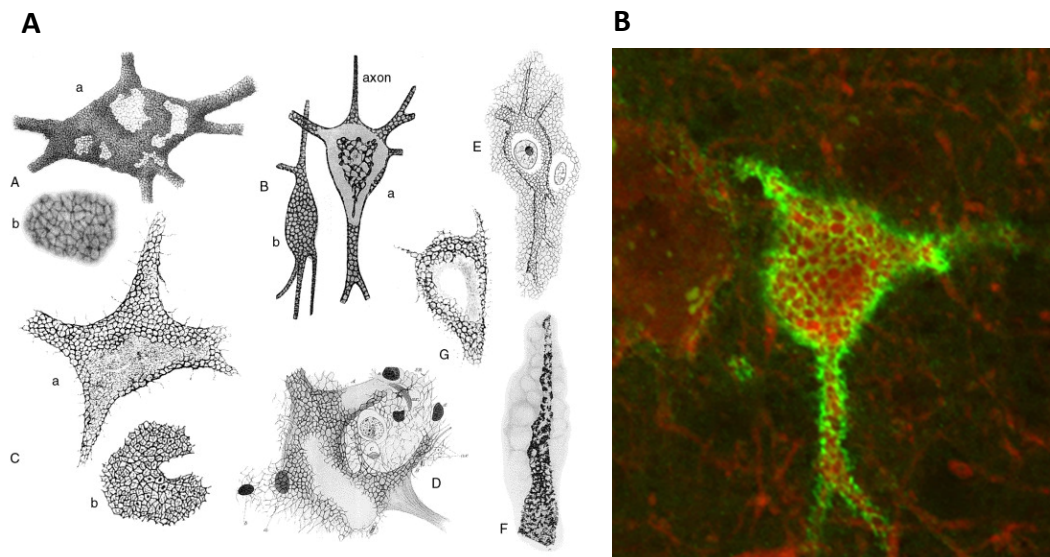
Figure 1.3:
A: Original drawings of the perineuronal nets from the papers of Camillo Golgi, Donaggio and Ramon y Cajal (reviewed by Vitellaro-Zuccarello et al., 1998), that are confirmed by modern confocal microscopy.
B: Confocal microscope image of PNN (green) surrounding a parvalbumin-expressing interneuron (red). Image by Lensjø et al. (2017).

1.2.1 Perineuronal net structure

The most common composition of PNNs is membrane-bound hyaluronic acid (HA), chondroitin sulphate proteoglycans (CSPGs) of the lectican family, a linking protein, and Tenascin-R (Tn-R) (Carulli et al., 2006; Celio and Blumcke, 1994; Deepa et al., 2006; Wang and Fawcett, 2012) (**Figure 1.4**). The unsulfated HA interacts with the CSPG core protein (brevican, neurocan, aggrecan and/or versican) through the lectican´s G1 domain (Yamaguchi, 2000). This structure is stabilized by a linking protein, which in most cases is the cartilage linking protein 1 (Ctrl1), and further strengthened by crosslinking the CSPG sidechains with Tn-R (Carulli et al., 2010; Kwok et al., 2011; Wang and Fawcett, 2012). Although most studied in PNNs, CSPGs are in fact mostly found in other loose types of ECM. However, the small fraction of CSPGs that are found in PNNs are bound so tightly by HA and Tn-R that PNNs form one of the most stable and aggregated forms of ECM in the brain (Deepa et al., 2006). The nets are most easily visualized using biotin- or fluorescent reporter-conjugated *Wisteria floribunda* agglutinin (WFA), selectively binding the CSPGs in PNNs (Hartig et al., 1992), and fluorescently labeled secondary staining binding to the WFA-conjugate.

The PNN component aggrecan has received much attention, and is thought to be an important part in the formation of CSPGs into PNNs, as it is expressed only from P14 with increasing expression until P150 (Yamaguchi, 2000). The expression of aggrecan is later, and more synchronized with the closing of critical periods than the other CSPGs (Yamaguchi, 2000). Aggrecan is also by far the CSPG with the highest number of chondroitin sulphate side chains (Galtrey and Fawcett, 2007). However, it seems that the link protein Ctrl1 could, in fact, be an equally important player in initiating the PNN formation, as its expression is highly correlated with the closing of critical periods (Carulli et al., 2010). Moreover, the link protein Ctrl1 seems

to be one of the most important components distinguishing the CSPGs in loose ECM from CSPGs in PNNs by binding them tightly to hyaluronan (Carulli et al., 2010; Romberg et al., 2013). However, genetic knockout of Ctrl1 only reduces the amounts of WFA positive PNNs (Carulli et al., 2010), while genetic knockout of Aggrecan completely abolishes WFA positive PNNs (Rowlands et al., 2018).
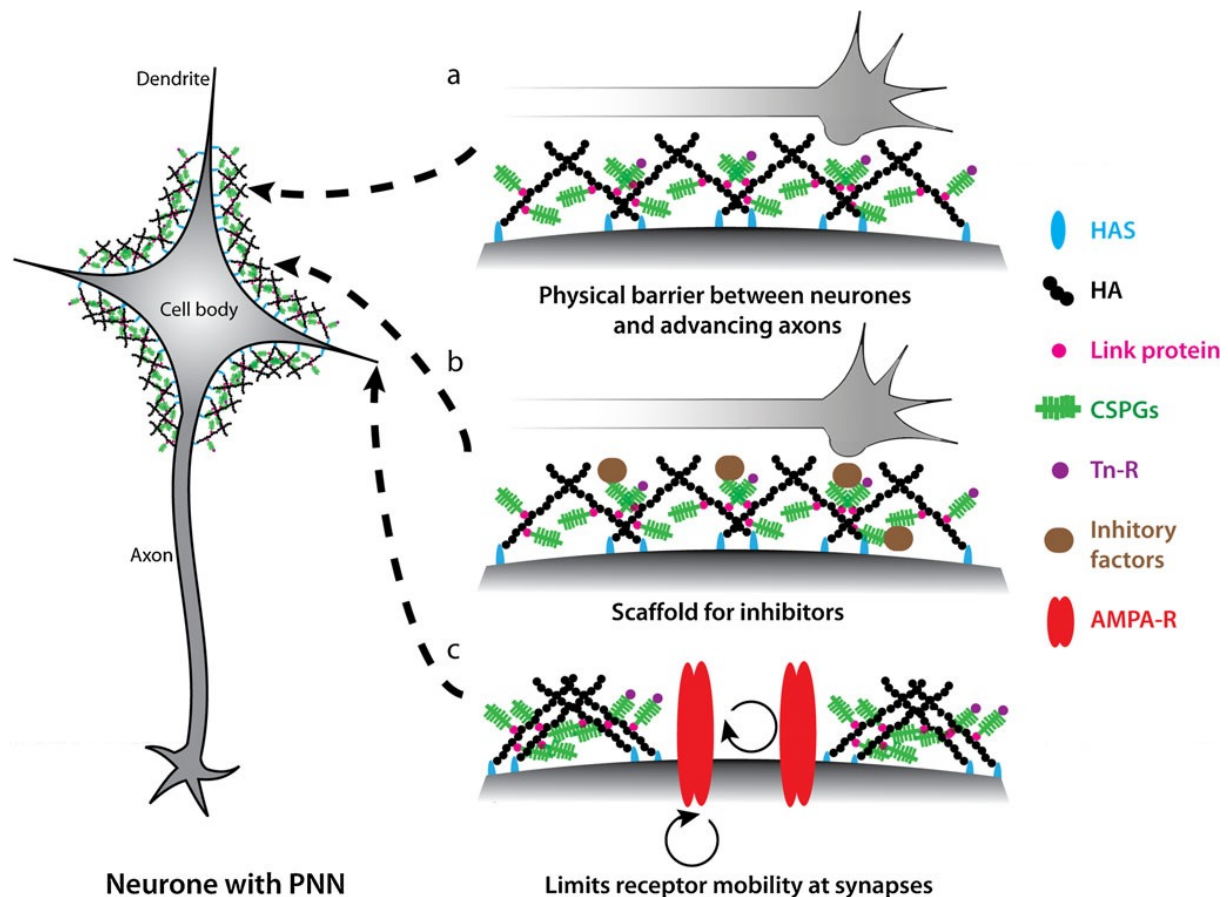
Figure 1.4: *This is the proposed structure of the PNN, showing how HA binds to linking proteins and CSPGs which crosslink with Tn-R to build a scaffold around the cell body. Figure by Wang and Fawcett (2012).*

1.2.2 Perineuronal net function

In mouse visual cortex, most of the neurons covered by PNNs are fast-spiking, parvalbumin-expressing (PV+), GABAergic interneurons in layer 2-5 (L2-5), regulating the activity of excitatory cells (Celio and Blumcke, 1994; Hartig et al., 1992; Lensjo et al., 2017; Pizzorusso et al., 2002; van 't Spijker and Kwok, 2017). Consistent with this, Faini et al. (2018) found that the majority of the PV+ cells in layer four of the primary visual cortex in the adult brain are enveloped by PNNs. Similarly, in the medial septum, the majority of fast-spiking, parvalbumin-positive neurons were ensheathed by PNNs (Morris and Henderson, 2000). A quadruple knockout of four different ECM components, three of which are part of PNNs, has recently shown that changes in ECM and PNNs alters the proportions of inhibitory and excitatory synapses, and increase total network activity in CA2 (Gottschling et al., 2019). These results

together imply that PNNs may have important functions in establishing adequate inhibitory input to cortical networks.

Unlike other types of ECM, PNNs in the primary visual cortex do not start to develop until around postnatal day 12-14 and keep developing for approximately ten days in rats and mice (Fawcett et al., 2019; Lensjo et al., 2017). In biology, critical periods are developmental stages characterized by heightened plasticity and sensitivity to external stimuli. In closing of critical periods, it is important to restrict the synaptic plasticity to establish a more stable synaptic environment. The PNNs act as a kind of scaffold to stabilize and restrict synaptic plasticity in the closing of the critical period (Lensjø et al., 2017). As reviewed by Wang and Fawcett (2012), the proposed functions of PNNs (shown in **Figure 1.4**) in this respect may be to act as a scaffold for neuronal growth inhibitors and restriction of AMPA-receptor diffusion at synaptic densities.

The tight organization of highly repetitive chondroitin sulphate chains in CSPGs accumulates negative charges, and renders the PNN microenvironment highly anionic. PNNs have been shown to decrease the diffusion coefficient of Ca^{2+} as a result of their charge (Hrabetova et al., 2009). In addition to hindering Ca^{2+} diffusion, it is thought that the charge enables the PNNs to buffer the positive ions, such as K^+ just outside the cell membrane (Hartig et al., 1999; van 't Spijker and Kwok, 2017; Wang and Fawcett, 2012). This idea is supported by a relatively recent study by Morawski et al. (2015), showing that ECM, and the polyanionic PNNs in particular, can capture cations and create anisotropic ionic diffusion in the local microenvironment. By capturing cations in the polyanionic nets, PNNs may shift the molecular gradients of biologically relevant cations (Morawski et al., 2015), and thereby perhaps facilitate high frequency firing. Furthermore, it seems that the polyanionic composition of PNNs may also provide neuroprotection against oxidative stress (Morawski et al., 2004). If PNNs indeed do buffer positive ions just outside the cell, this should effectively increase the distance between the negative intracellular solution and the positive extracellular ions. From the definition of a capacitor, increasing the distance between the conductive compartments should lower the capacitance of PNN neurons. Consistent with this idea, Tewari et al. (2018) found a significant increase in membrane capacitance, and consequently lowered maximum firing frequency, after removing PNNs around peritumoral fast-spiking interneurons in cortex, using a tumoral mouse epilepsy model.

As there are so many proposed functions of PNNs on properties that are crucial to proper brain function, it is not surprising that PNNs have also been implicated in several neurological disorders (Pantazopoulos and Berretta, 2016). Although the results in this field are inconclusive, some of these disorders are discussed in section 4.2.

1.2.3 PNN removal

Previous research clearly suggests the PNNs play a big role in balancing synaptic, and network plasticity, as well as having potential effects on the electrophysiology of single cells and networks. However, the full specter of mechanistic and functional roles of PNNs remains elusive. The most common way to study the PNNs is by comparing different parameters, such as learning or cell excitability before and after PNN removal. Previously, and still today, the most used method to remove PNNs has been through enzymatic digestion by the bacterial enzyme chondroitinase ABC (chABC). The original chondroitinase ABC purified from *Proteus vulgaris* contains a mix of endo- and exolyases chABC 1 and chABC 2 (Hamai et al., 1997), which both cleave HA, CSPGs and some dermatan sulphates (Tester et al., 2007). According to Hamai et al. (1997), protease free chABC should only contain chABC lyase 1 and is now considered to be the gold-standard of chABC. As shown in **Figure 1.5**, chABC cleaves the chondroitin sulphate chains of CSPGs in both PNNs and other ECM by enzymatic depolymerization of the carbohydrate chains (Bruckner et al., 1998). The enzyme is not affected by the aforementioned distribution of CSPGs (Deepa et al., 2006), but cleaves the chondroitin sulfate chains of CSPGs in all ECM. Because the CSPGs in loose ECM are more diffuse and have less distinctive functions than in PNNs, the effects of cleaving CSPGs in ECM are usually neglected, and the results observed after enzymatic degradation are typically attributed to PNN function. ChABC has also been found to diminish hyaluronan and tenascin-R in dissociated hippocampal neural culture (Dityatev et al., 2007), although this has not been reported by *post mortem* analyses in tissue slices after *in vivo* treatment with chABC (Bruckner et al., 1998; Deepa et al., 2006).
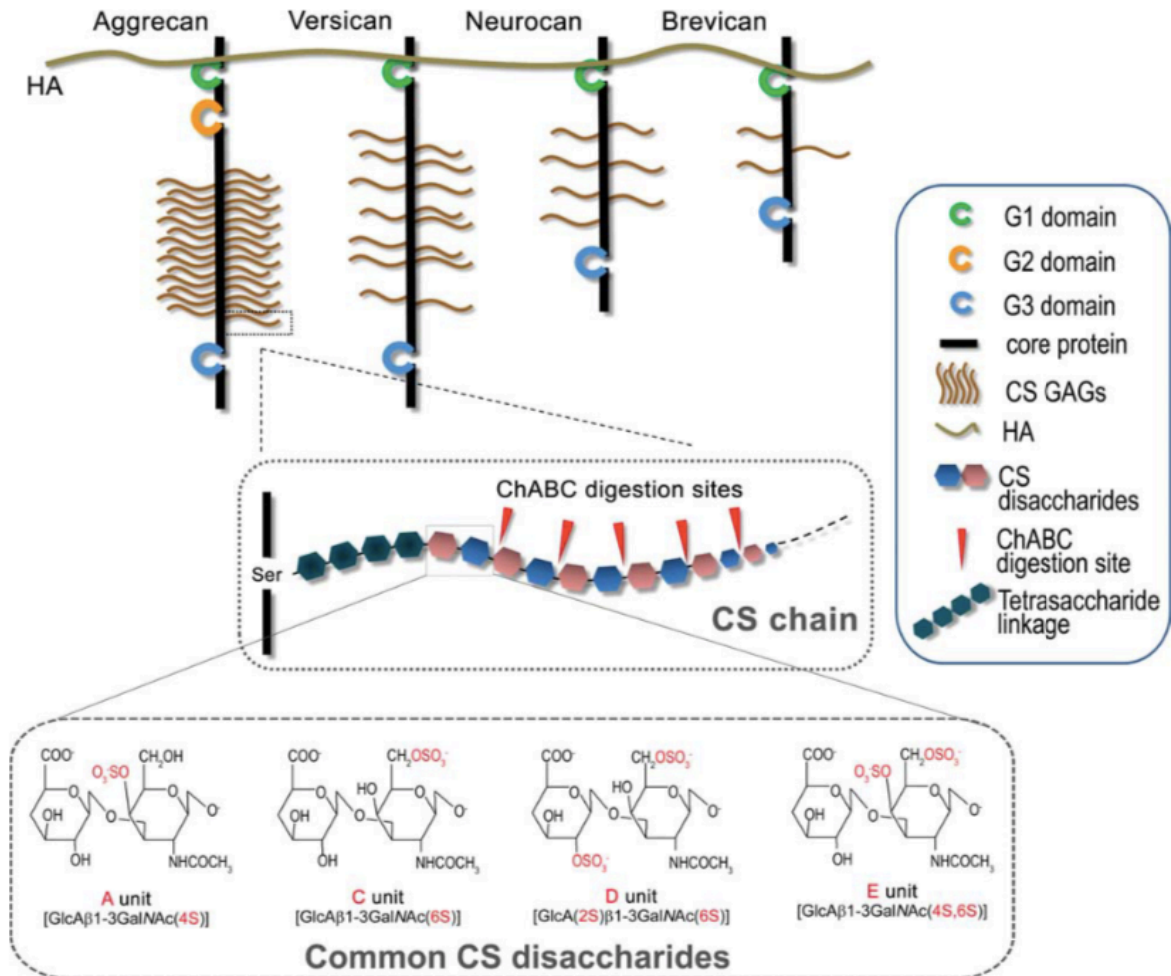
Figure 1.5: *ChABC targeting the chondroitin sulfate sugars for degradation. Figure by Kwok et al. (2011)*

Although enzymatic degradation by chABC is by far the most common way to remove PNNs, other methods using genetics have emerged in the last decade. The current study has made use of genetically modified mice (B6(Cg)-ACAN[tm1c(EUCOMM)Hmgu>/Jwfa]), henceforth referred to as AcanKO mice, in which the gene encoding for the PNN and cartilage component aggrecan has been knocked out specifically in the CNS (Rowlands et al., 2018). Rowlands et al. (2018) have shown that these AcanKO mice are unable to aggregate other PNN components as well, and are effectively deficient of PNNs. The AcanKO mice are bred from Acan-lox mice in which the aggrecan gene is a functional FLEX-switch (see next section) that have been crossed with mice expressing the recombinase Cre only in the CNS.

As mentioned, PNNs are proposed to have an ion buffering action, and there seems to be a link between the PNNs and the capacity for high-frequency firing in PV$^+$ cells. However, there are currently conflicting results on how PNN-removal changes the excitability and electrophysiology of PV$^+$ cells (Balmer, 2016; Chu et al., 2018; Dityatev et al., 2007; Faini et al., 2018; Favuzzi et al., 2017; Tewari et al., 2018). According to Chu et al. (2018), PNN removal by chABC treatment increased (depolarized) the resting membrane potential (RMP) and decreased the input resistance of PV$^+$ interneurons. This effect was not seen in low threshold

spiking interneurons (Chu et al., 2018). The different approaches to remove PNNs, and the brain areas studied vary between these papers, and this makes it difficult to compare the results. However, most papers have used tissue slices from young animals (<P35) when recording. Knowing that the firing pattern of different neurons changes with maturation (Petilla Interneuron Nomenclature et al., 2008), and that PNNs are not fully developed at this early stage (Sigal et al., 2019), it is imaginable that recordings from more mature slices, as used here, may yield different results.

1.3 AAV-FLEX viral vector transduction

Over the recent years, adeno-associated viruses (AAVs) have emerged as valuable tools serving as vectors for gene delivery in research and gene therapy (Challis et al., 2019) (**Figure 1.6**). AAVs are non-pathogenic, non-cytotoxic and induce low immunogenicity. The AAV viruses have single stranded linear DNA with two open reading frames (Rep and Cap) that are flanked by inverted terminal repeats (ITRs). The ITRs base pair to allow synthesis of the complementary strand, and thereby enabling transcription of the Rep and Cap genes encoding for proteins essential for the AAV life cycle (Deyle and Russell, 2009). The constructs and the procedure for retro-orbital injection used here is specified in 2.2 Virus Preparations.
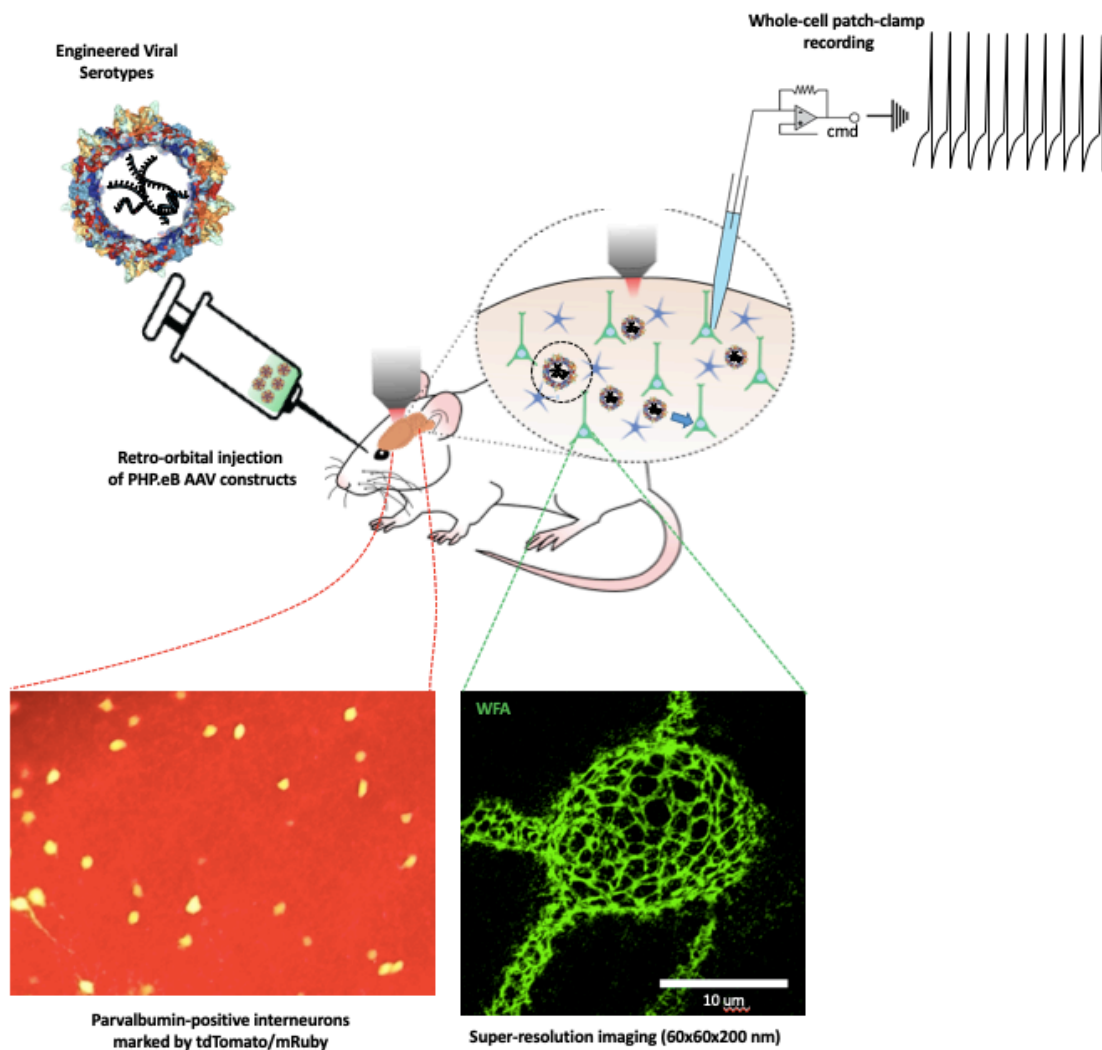
Figure 1.6: Showing how AAV vectors can be used for the experiments intended for this study (see 1.4 Aims of study).

When preparing a recombinant AAV transfer plasmid (rAAV), a transgene cassette usually replaces the Rep and Cap genes between the two ITRs, and the replication genes are provided by co-transfection of a helper plasmid containing Rep and Cap (Deyle and Russell, 2009). In rAAVs, the ITRs are also in *trans* configuration to avoid integration into the host genome. A common outcome of AAV infection is thereby the formation of double-stranded episomes in the nucleus. These are not integrated in the host genome, but they are long-lived and can provide stable transcription of the viral transgenes over long periods *in vivo*, even in non-dividing cells (Deyle and Russell, 2009).

One way of increasing target specificity, and to reduce undesired infections of rAAV transduction, is to combine cell type-specific Cre-expression with a FLEX-switch (**Figure 1.7**) in the rAAV (Atasoy et al., 2008; Saunders et al., 2012). Cre-recombinase is an enzyme that performs recombination between two homotypic lox-sites. Depending on the orientation of the lox sites, the sequence between two lox-sites may be inverted, excised or, if lox-sites are

present in the host genome and a donor transgene flanked by lox-sites is provided, the donor gene can be inserted. For this study, mouse lines selectively expressing Cre-recombinase in GABAergic PV[+] interneurons have been used, and the FLEX-switch will therefore only be activated in these cells. The FLEX-switch used in this study consists of a transgene cassette (encoding either tdTomato or mRuby) flanked by two pairs of antiparallel lox-sites; one pair of loxP and one pair of lox2272 (Atasoy et al., 2008) (see 2.2.1 for specifications of constructs). The transgene cassette is inverted relative to its promoter, and must be flipped to enable transcription (**Figure 1.7**). However, when the gene is flipped, another round of recombination could invert the gene back to the inactive orientation. By having two pairs of lox-sites, the first recombination will leave one lox-pair in parallel on one side of the transgene. With a homotypic lox-pair in parallel, separated only by a lox-site of the other pair, a second round of recombination will instead excise two of the lox-sites, leaving the transgene in the active orientation flanked by a heterotypic pair of lox-sites; one loxP and one lox2272 (**Figure 1.7**) (Saunders et al., 2012). Cre-lox recombination can only happen between homotypic lox-sites, and the transgene is therefore left in the active orientation yielding stable gene expression only in rAAV-FLEX infected cells also expressing Cre (Atasoy et al., 2008).
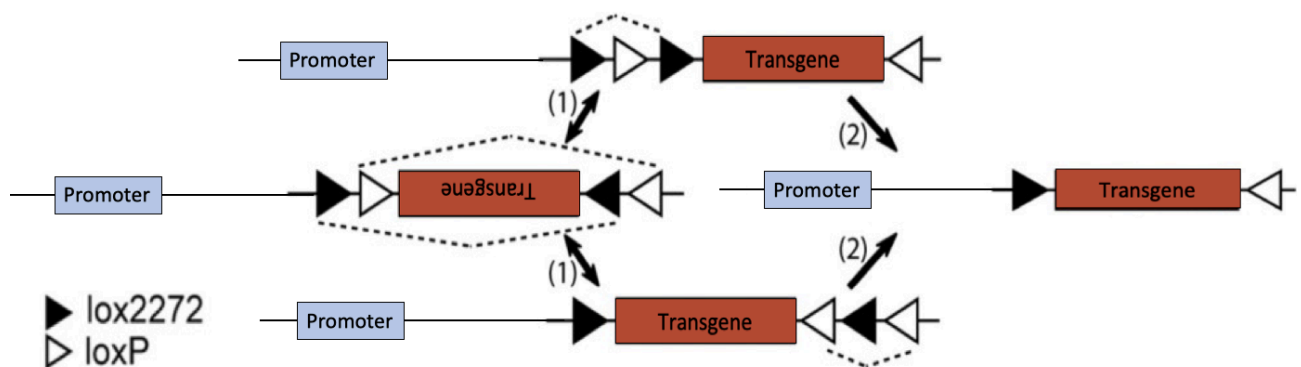
Figure 1.7: The FLEX-switch allowing specific, and stable activation of a transgene by two rounds of Cre-lox recombination. Figure modified from Atasoy et al. (2008).

1.4 Aims of the study

Currently, there are conflicting results on excitability changes after PNN removal (Balmer, 2016; Chu et al., 2018; Faini et al., 2018; Favuzzi et al., 2017; Hayani et al., 2018; Tewari et al., 2018). Because different methods have been used to remove the PNNs, I aimed to dissect these differences by comparing different methods of removing PNNs. Specifically, the view on chABC has changed, and the general opinion is now that chABC is a harsh and imprecise enzyme, and more selective, elegant and physiological methods are sought for. It is clear that chABC indeed removes PNNs, and that PNN removal by chABC gives the same plasticity changes as PNN removal by more elegant knockout experiments (Carulli et al., 2010; Romberg et al., 2013). However, to my knowledge, there have been no control experiments on how chABC itself affects cellular electrophysiology. Therefore, my aim with this study was to investigate if PNN removal changes the electrophysiology of PV[+] interneurons in the primary

visual cortex of adult (>P100) mice, and whether chABC treatment, either *in vivo* or *ex vivo* contributes to potential changes measured in acute slices. To achieve these objectives, I aimed to:

- Perform whole-cell patch-clamp recordings of PV$^+$ interneurons in the primary visual cortex of adult (>P100) WT (control) and aggrecan knockout mice to investigate if the absence of PNNs causes any changes in membrane capacitance, maximum spike frequency and/or sEPSCs
- Perform local the primary visual cortex *in vivo* injections of the bacterial enzyme chABC in adult WT and AcanKO mice, and repeat the whole-cell patch-clamp recordings to see if chABC treatment differs from AcanKO with respect to electrophysiology
- Compare the effects of *in vivo* injections versus acute *post mortem* degradation by slice incubation in chABC
- Confirm cell viability and PNN-state by *post patch* fluorescent confocal microscopy

By comparing my recordings to previous recordings done in WT mice with PNNs, and recordings from other electrophysiology studies on PNN removal, I wished to implement this as a control experiment ensuring that any electrophysiological changes are caused by the removal of PNNs, and not by the chABC treatment. However, because of the SARS-Cov-2 pandemic, the laboratories were closed before I could perform the chABC experiments and the *post patch* imaging. Therefore, only the control versus AcanKO experiments are presented in this thesis, along with an introduction and a methodological discussion on chABC treatment for future experiments. The chABC experiments, histology and imaging are also described in the appendix (see 6.4 Planned experiments) although not performed.

2 Materials and methods

2.1 Approvals and research animals

All experiments were performed at the Institute of Basic Medical Sciences (IBM), University of Oslo, Norway, and were approved by the Norwegian Food and Safety Authority (Mattilsynet) and the Norwegian Animal Research Authority (FDU) prior to project commencement. All participating parties had completed courses in experimental animal research ahead of project initiation, and hold an animal research certificate (FELASA C or similar), as required.

22 c57bl6 mice were sacrificed and recorded. However, the recordings from eight of these mice did not meet the predetermined quality criteria, and were therefore discarded. The recordings were either from PV^{Cre} control mice with wild type alleles for PNN components (B6;129P2-Pvalb$^{tm1(cre)Arbr/J}$ from Jackson Laboratories) (Hippenmeyer et al., 2005), or from aggrecan knockouts from birth (B6(Cg)-ACAN$^{tm1c(EUCOMM)Hmgu>/Jwfa}$) (Rowlands et al., 2018). Recordings of 14 c57bl6 mice were used. Of these, seven were PV^{Cre} and seven were AcanKO.

All mice were locally kept and maintained at the animal facility at the Department of Comparative Medicine, IMB, University of Oslo. All animal housing, handling and sacrifice were in line with regulations set by the European Union and the FDU. The mice were kept in standard cages (Techniplast Sealsafe Plus GM500), with a 12-hour light cycle and *ab libitum* access to food and water.

2.2 Virus preparations

2.2.1 Production of PHP.eB AAV9-FLEX viruses

The viruses used for the experiments were produced by Sverre Grødem and Guro Vatne at the Department of Biosciences, UIO. All procedures for the production, purification and titration of our two viruses were strictly followed as described in (Challis et al., 2019). A summary of the protocol will follow here, but for full procedure see the cited protocol paper. Two different recombinant AAV plasmids with the same core functions were used to make two AAV9 viruses; PHP.eB AAV9-FLEX-tdTomato and PHP.eB AAV9-FLEX-mRuby respectively. The plasmid pAAV-FLEX-tdTomato was provided to us by Edward Boyden (Addgene plasmid # 28306; http://n2t.net/addgene:28306; RRID: Addgene_28306), and the plasmid AAV pCAG-FLEX-mRuby3-WPRE was provided to us by Rylan Larsen (Addgene plasmid # 99279; http://n2t.net/addgene:99279 RRID: Addgene_99279). Both viruses yield widespread and targeted gene expression of red fluorescent proteins (tdTomato and mRuby) selectively in PV$^+$ neurons expressing Cre recombinase. Selective marking of all PV$^+$ neurons made targeting neurons of interest during patch-clamp recordings much more efficient. In our experience, all of the fluorescently labeled PV$^+$ neurons in the primary visual cortex were also fast-spiking.

The first part of the virus production protocol is a triple transient transfection of HEK293 cells in cell culture flasks. For this step, the cells are transfected with three different plasmids. The

pHelper plasmid contains adenoviral genes necessary for replication, while pUCmini-iCAP-PHP.eb contains the Cap gene for the PHP.eB serotype specifically infecting neurons in the CNS (Challis et al., 2019). pUCmini-iCAP-PHP.eB was provided to us by Viviana Gradinaru (Addgene plasmid #103005; http://n2t.net/addgene:103005; RRID: Addgene_103005)(Chan et al., 2017). The third plasmid contains the transgene – tdTomato or mRuby as specified above. Following the transfection, the next steps involve harvesting of media and cells to collect as much virus as possible before the purification. The media is collected at two different time points to maximize cell health and virus yield, and the media is combined with the harvested cells. Through several steps of centrifugations and buffer/enzyme additions, the volume is reduced as the virus becomes more concentrated in the preparations leading to purification. During purification, the virus is concentrated further in a density gradient ultracentrifugation step, before being extensively purified and filtered through several more steps of shorter centrifugations. Having successfully produced and purified the viral preps, each viral prep is titered by qPCR to determine the number of viral particles per ml. The viruses can be stored at 4°C for up to 6 months (Challis et al., 2019).

2.2.2 Retro-orbital virus injections

All the viral injections were performed by my supervisor, PhD candidate Sverre Grødem. As I was about to proceed with injections by myself, the lab was shut down due to the SARS-Cov-2 pandemic, and I was therefore unable to perform injections myself. The viruses were injected retro-orbitally, as described by Challis et al. (2019), and briefly summarized here. The mice were deeply anesthetized with 5% isoflurane mixed with air, unresponsive to toe-pinch, and anesthesia maintained by 1.5-2% isoflurane through a face mask. The procedure was quick and completed within 2 min after stable anaesthesia was achieved. All the injections were successful. A dosage of $5*10^{12}$ vector genomes were loaded in an insulin syringe, and prepared for injection. With one hand, the skin above and below the eye was pulled back to expose the whole eye and eye socket. With the other hand, the syringe was carefully guided under the eye to the back of the socket, through the conjunctival membrane and the virus was slowly injected into the retro-orbital sinus. After successful injections, no fluid should leak from the eye, and only minimal amounts of blood should be observed. Immediately after successful injection, the injected eye was instilled with 1 drop of 0.5% Alcaine ophthalmic solution (ALCON Canada Solutions), and the injected eye was routinely checked over the next few days.

2.3 Patch-clamp experiments
2.3.1 Acute brain slice preparation

Acute brain slices are *ex vivo* slices from brains that are extracted and cut immediately before the experiment is performed. They are used within hours after preparation to obtain slices that are physiologically as close as possible to the *in vivo* situation (Carter and Shieh, 2015). Traditionally, acute brain slices are obtained from young mice (<P30), because they are more resilient to tissue damage. Young animals also have a more immature metabolic state that is

more compatible with *ex vivo* survival than slices from adult animals. However, using new protocols from described in (Ting et al., 2018) and as described below, 350 μm thick acute slices from much older animals (>P120) were prepared, in which the PNNs and neural tissue are fully developed and matured. In these slices, fluorescently labeled PV⁺ inhibitory neurons in the primary visual cortex were identified, and voltage and currents were recorded using a whole-cell patch-clamp configuration.

All animals were anesthetized with ~5% isoflurane (Baxter AS, Oslo, Norway) mixed with air until they were unconscious. While unconscious, they were injected with an overdose of Pentobarbital sodium (100 to 200 μl, 400mg/ml, Le Vet Pharma B.V, The Netherlands) intraperitoneally. When deeply anesthetized and all reflexes were completely absent, the animals were transcardially perfused with ice cold, oxygenated (95% O_2, 5% CO_2) NMDG-HEPES aCSF solution for two minutes at about 10ml/min. Following perfusion, the mice were decapitated and the brains were dissected out and incubated in ice cold, constantly oxygenated NMDG-HEPES aCSF for one minute. The cerebellum and approximately 2-3 mm of the rostral cortex were cut off using a razor blade, before the brains were glued and mounted to the cutting platform of a vibratome. Using a Leica VT1200 vibratome slicer (Leica Biosystems, USA) the brains were cut caudo-rostrally in 350 μm slices, and hemisected to make 6-8 coronal half-brain slices of the primary visual cortex per mouse. For optimal slice health, the perfusion, dissection and slicing must be completed within 15 minutes after initiating the perfusion.

Following slicing, all slices were transferred into a beaker with 150 ml NMDG-HEPES aCSF kept at 32°C under constant oxygenation. A sodium spike-in protocol (see appendix 6.4.1 for full protocol) ensured a gradual adaptation to higher sodium concentrations before transfer into the holding buffer. After completing the 25 min sodium spike-in, all slices were transferred into a new beaker of HEPES-holding aCSF kept at room temperature (20-25°C) under constant oxygenation. The slices were left for recovery for at least one hour before the patch-clamp recordings could begin.

2.3.2 Whole-cell recording

For the patch-clamp recordings, a slice was transferred from the holding beaker into the patch-clamp chamber. The chamber is kept at 31-33°C and superfused with constantly oxygenated recording aCSF at a rate of ~2ml/min. Using the threads of the slice holder, and the shape of the hippocampal ventricles as visual reference, recordings were limited to the primary visual cortex layer 2-6 (**Figure 2.4**). When a good and healthy-looking PV⁺ cell was identified, using both the red fluorescence of tdTomato/mRuby and the morphology seen using an infrared differential interference contrast (DIC) microscope (Zeiss Axioscope, 40X water-immersion 0.75 N.A objective), the pipettes were prepared and filled. Firepolished borosilicate glass pipetes (GB200-8P, Science Products GmbH, Hofheim, Germany) with a resistance of 2.8-5.8 MΩ were pulled, using a P1000 pipette puller (Sutter Instruments,

Novato, CA, USA). They were filled with an intracellular solution (see appendix 6.2.5) with Alexa Fluor™ 488 hydrazide (A10436; Invitrogen by Thermo Fisher Scientific); first backfilled by negative pressure, before adding the rest with a long pipette tip. The Alexa Fluor™ dye is added to the intracellular solution immediately before use. The filled pipettes were then fitted over a silver electrode attached to a head stage controlled by a Luigs & Neumann SM-5 9 micromanipulator (**Figure 2.1**). The glass pipettes were added a positive pressure of 100-115 millibar to avoid clogging by external dust or particles. Using a camera (Hamamatsu C2400) attached to the DIC microscope and a CRT video monitor, the pipettes were visually guided to the surface of the brain slice, before adjusting pipette offset and reading the pipette resistance. Adjusting pipette offset compensates for voltage offsets arising from the pipette, electrode and amplifier by setting the baseline current to zero, using the bath electrode as reference. Adding the voltage offset to the command voltage will adjust the output current so that there is zero current flow at command voltage zero. The pipettes were then navigated onto the cell membrane of the PV⁺ cell and, by using light suction, an electrical giga-ohm seal with the membrane was obtained. By applying a sharp pulse(s) of firm suction, the membrane patch in the pipette was ruptured while still maintaining a tight electrical seal, to obtain the whole-cell recording mode (**Figure 2.2**). In whole-cell mode, recordings of membrane potential, membrane capacitance, firing frequencies and spontaneous excitatory postsynaptic currents (sEPSCs) were done by recording by recording in both voltage- and current-clamp mode.
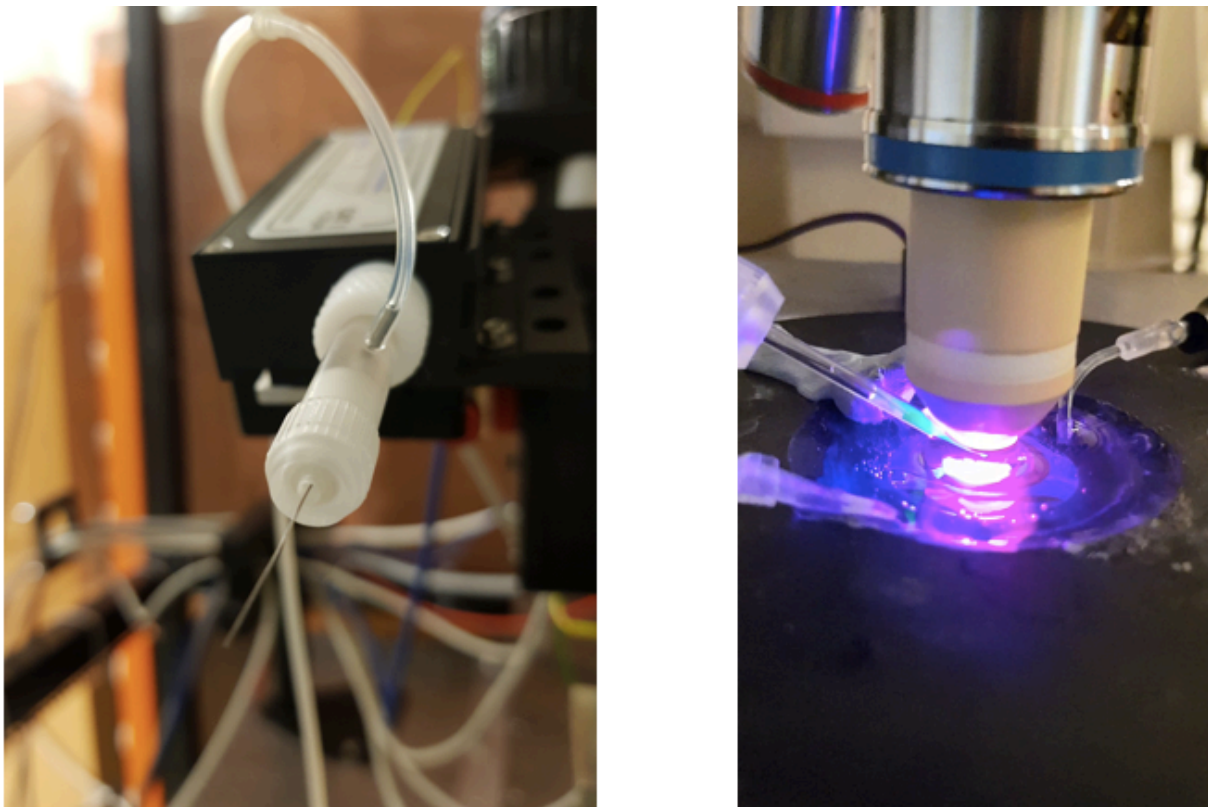
Figure 2.1: The silver electrode mounted onto the head stage (left), and the electrode with a filled pipette during recording (right).

Each cell was recorded using two different recording protocols; one current-clamp protocol and one voltage-clamp protocol. In the current-clamp protocol, bias current was injected to keep the membrane potential at ~ -65 mV. They were injected with 1000 ms square step currents increasing with 50 pA increments from -350 pA to 1100 pA while reading the voltage changes resulting from the current injections (**Figure 2.3**). To calculate capacitance, input resistance and voltage deflection, each increasing current step is preceded by a hyperpolarizing step for 500 ms. The cells are allowed to rest in pauses between each current injection. The current injection protocol is quite hard on the cells, and at the end of the protocol, some of the cells exhibited baseline hyperpolarization and reduced AP amplitude. These cells were excluded from the analyses. From the current-step protocol, recordings of approximate rheobase, maximum AP frequencies, and adaptation were obtained. Input resistance and membrane capacitance was also calculated from the hyperpolarizing step. With the voltage-clamp protocol, the membrane potential was clamped to -70 mV and the currents from synaptic inputs and sEPSPs were recorded for 3 minutes.
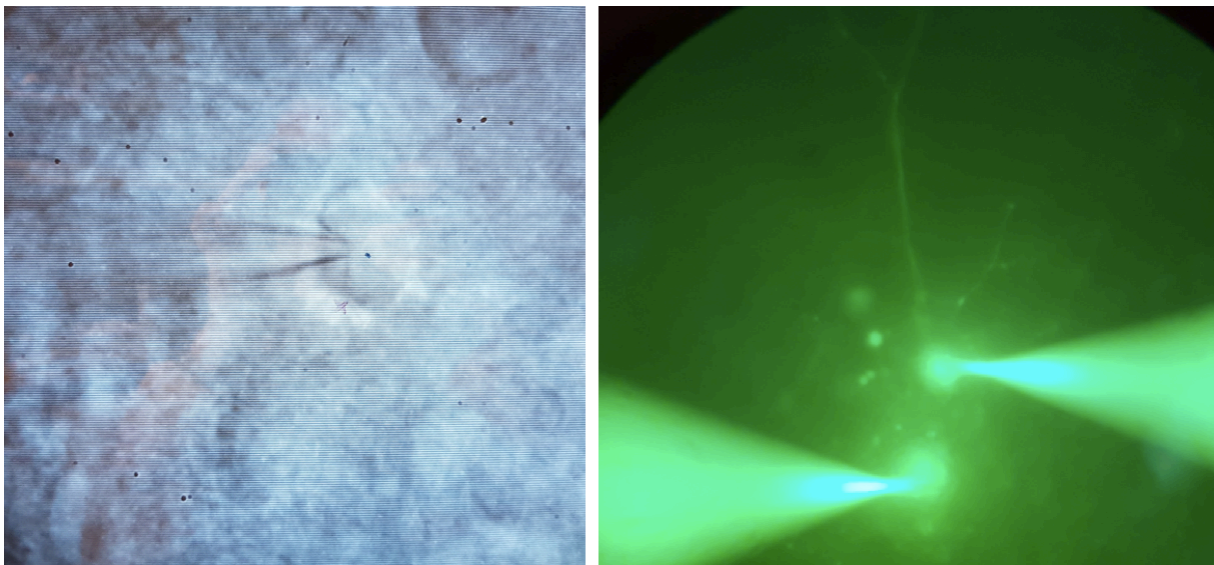
Figure 2.2: A cell ruptured into whole-cell mode viewed on the CRT video monitor (left), and the fluorescent internal solution filling the patched cells in a dual patch (right). Images by Sverre Grødem.
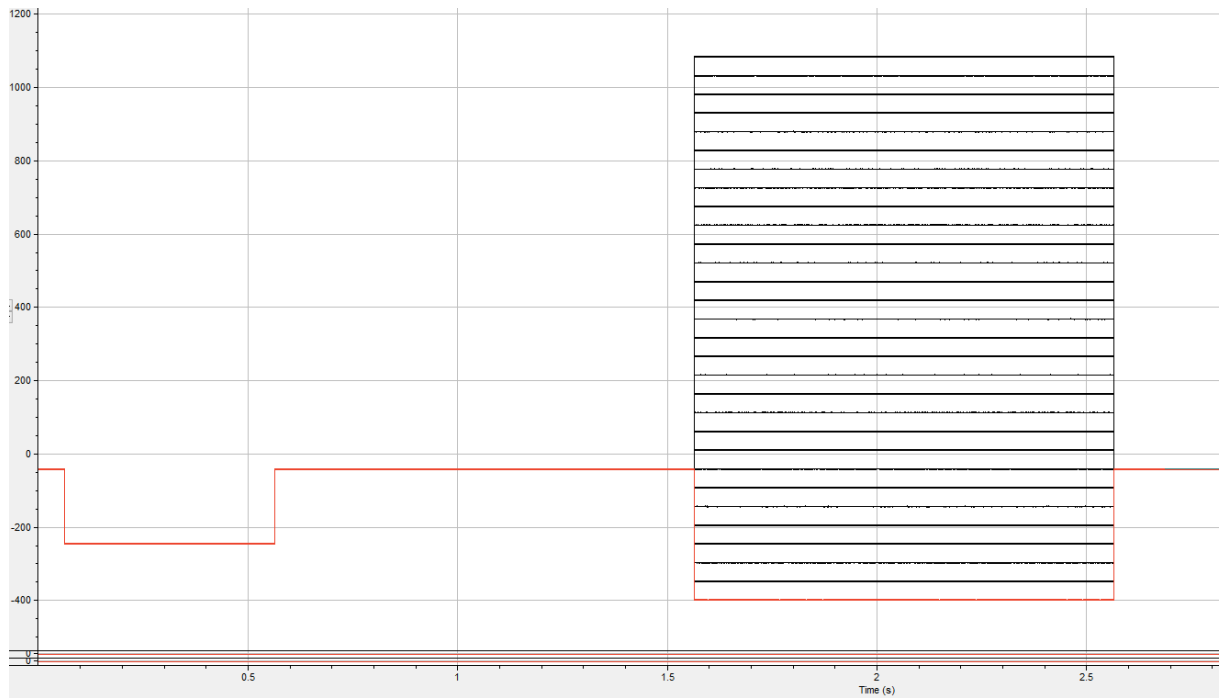
Figure 2.3: *Current clamp square step current injection protocol starting at -350 pA increasing to 1100 pA over 30 sweeps. Each sweep also has a hyperpolarizing step to -250 pA. The first sweep is marked in red. In the recording shown here, the bias current injected to keep the cell at -65 mV was -40.2 pA, and the step intensities are measured from this baseline.*

All data was amplified (Multiclamp 700B, Molecular Devices) and digitized (Axon Instruments 1550B, Molecular Devices) using Clampex 11.0.1 Software (pClamp™ Software Suite, Molecular Devices) and Mulitclamp 700 B (pClamp™ Software Suite, Molecular Devices) software.

After the recordings, each cell was kept in whole-cell mode to a total of ~15-20 minutes to allow the intracellular solution with the green dye to completely fill the cells with all their processes. Then, the pipettes were retracted very slowly to allow the cell membrane to reseal.
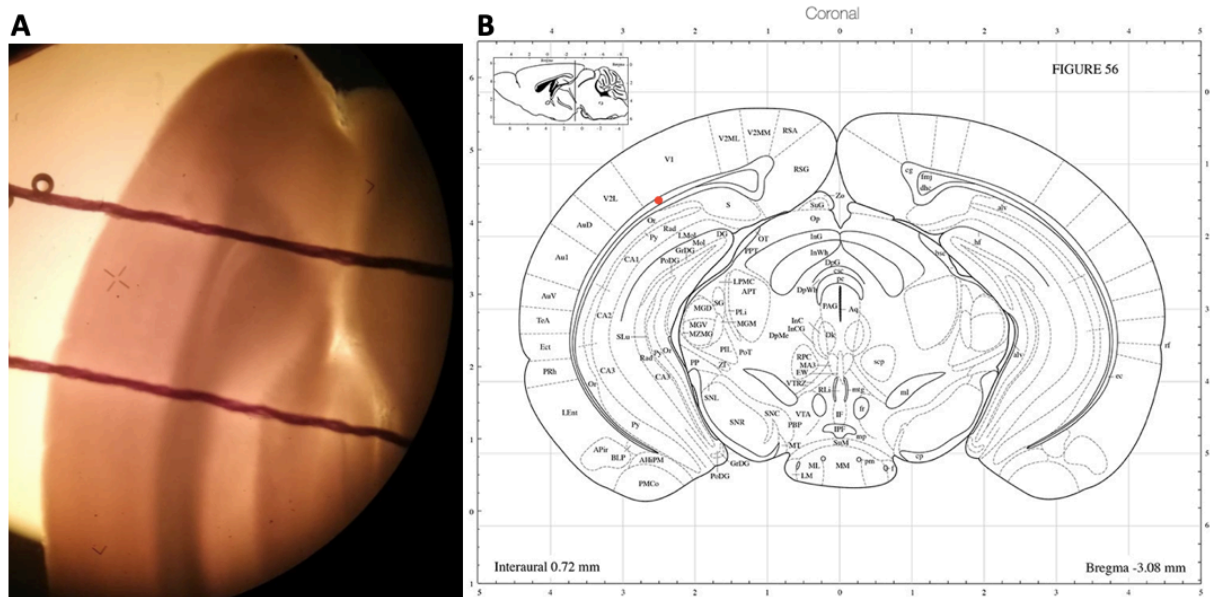
Figure 2.4: A: Approximate limitation of primary visual cortex, using the filaments of the slice holder. Conformation of "approved" boundaries using the 4X objective with light microscopy. Figure B by Paxinos (2001)

2.4 Data analyses

2.4.1 Current-clamp analysis

All electrophysiological data obtained in current-clamp was analyzed using custom pyABF (Harden, 2020) and eFEL scripts (Blue Brain Project, EPFL Revision 760ec492) in Python 3.7. All the resulting graphs and tables for each cell were then manually evaluated and recordings that did not satisfy the predetermined requirements (see Results) were discarded, until all the remaining cells fit the criteria described in the results. Only 13 of 41 cells in the control group, and 13 of 36 cells in the AcanKO group fit perfectly within the criteria and were included in the final analyses and results.

The current-clamp result graphs showing capacitance and spike frequency (**Figure 3.3** and **3.5**) were made in Prism 8 (GraphPad Software). The current-clamp statistics were also performed and calculated in Prism 8; Cm estimates were evaluated using an unpaired t-test, while the frequency data was evaluated using a two-group Kolmogorov-Smirnov test.

2.4.2 Voltage-clamp analysis

For the voltage-clamp analysis, the recordings for each cell was manually analyzed in Clampfit 11 Software (pClamp™ Software Suite, Molecular Devices) using the Event detection and Template matching. Each voltage-clamp recording resulted in a separate file containing all detected events. These files were then further analyzed through a custom script in Python 3.7. The number of detected events in each recording was counted in the script and sorted into good and bad sEPSC matches. Only the good sEPSCs are included in the analysis. Additional information about mean sEPSC amplitude and frequency is also included here. The sEPSC data was manually sorted into control and AcanKO, and the two groups were compared using unpaired t-tests in Prism 8 (GraphPad Software). Voltage-clamp data of sEPSC count,

amplitude and frequency (**Figure 3.6**) were visualized using graphs from Prism 8 (GraphPad Software).

2.5 Other Experiments

In addition to the experiments described here I had also planned experiments for comparing the results from control and AcanKO mice with different treatment regimens of chondroitinaseABC, and also performing post-recording fluorescent imaging analyses. These experiments were scheduled to be done in March/April, but could not be performed due to the SARS-Cov-2 pandemic. Due to all the time invested in the careful planning and for completeness of the thesis project I present them in appendix 6.4.

3 Results

Only fluorescently labeled PV$^+$ cells (**Figure 3.1**) with a stable electrical seal > 1 GΩ were ruptured into whole-cell mode. Of these cells, only those with a stable Vm > -50 mV and access resistance < 30 MΩ (measured in Clampex 11.0.1, pClamp™ Software Suite, Molecular Devices) were recorded. As described by Kandel et al. (2012a), most neurons have resting membrane potentials between -50 and -80 mV and often have action potential thresholds between -40 and -50 mV. Cells with RMP more depolarized than -50 mV are therefore regarded as abnormal or damaged. Empirically, the PV$^+$ neurons also have lower input resistances than other cell types, and the limit was set at 30 MΩ. Fast-spiking neurons were defined as neurons with maximum spiking frequency above 300 Hz with no adaptation. After initial analysis in Python, additional cut-off criteria were applied. The current clamp protocol was quite hard on the cells and many cells exhibited baseline hyperpolarization and reduced spike amplitudes towards the end of the protocol. Cells that showed signs of baseline hyperpolarization, had discontinuous or unstable f-I curves or a minimum spike amplitude below 50 mV were excluded from the results. 28 of the recorded control cells, and 23 of the recorded AcanKO cells violated the criteria in one or more ways, and were discarded.
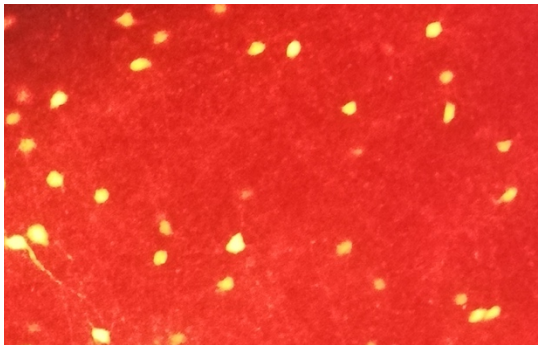
Figure 3.1: *Fluorescently labeled PV-cells (yellow). Imaged with a 10X 0.45 N.A. (CFI Plan APO) objective*

3.1 PNNs decrease the membrane capacitance of PV$^+$ FS -neurons

To illustrate the importance of the method used to calculate membrane capacitance, results of both the voltage-clamp step (VC-step) protocol in the Membrane Test function embedded in Clampex 11.0.1 (Molecular Devises) and calculations of *Cm* from a current-clamp step (CC-step) protocol are included. In the CC-step protocol, Cm is calculated from the hyperpolarizing step in each sweep (**Figure 2.3** & **Figure 3.2**), and these calculations are averaged for each cell. To measure capacitance, the change in membrane potential (ΔVm) resulting from the injected current (I$_{ext}$) is expressed by two exponentials (black line A$_1$ and A$_0$) where t is the time since the current injection and τ is the time constant (Golowasch et al., 2009). Solving **equation 3** for the slowest exponential will yield τ$_0$, and capacitance can be calculated from τ$_0$ = R$_m$C$_m$. Although yielding different numerical values for total membrane capacitance, a significant increase in Cm from control to AcanKO mice was found in both cases (**Figure 3.3**). An increase of more than 20 % (26% in VC and 22% in CC respectively) was measured in the AcanKO mice,

from 55.0 ± 10.7 pF (CC-step) in the control mice to 67.3 ± 14.1 pF (CC-step) in the AcanKO mice (p < 0.05).
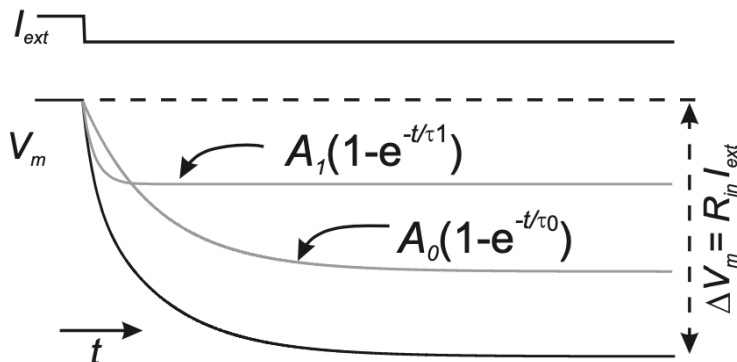
Figure 3.2: *Calculations of membrane capacitance from a hyperpolarizing step current. The different exponentials (A_1 and A_0) for membrane potential represent voltage equalization between cellular compartments, and the exponential with the slowest time constant is used for capacitance calculations. The slowest exponential represents the charging of the membrane capacitor. Figure by Golowasch et al. (2009)*
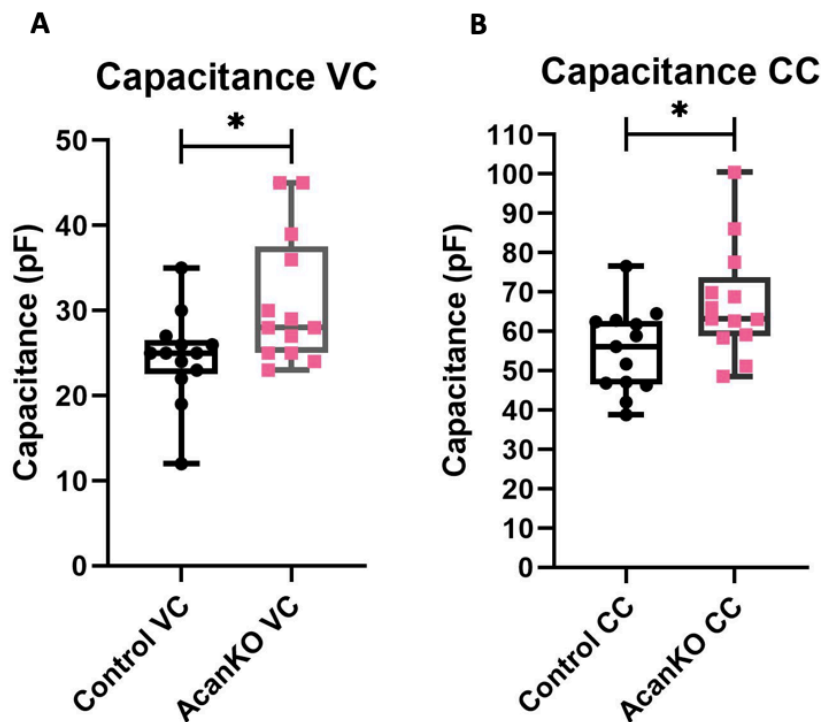
Figure 3.3: Measuring total membrane capacitance in AcanKO versus controls
Comparing measurements of total capacitance by voltage-clamp (A) and current-clamp (B) protocols. Both figures show measured total membrane capacitance in picofarad (pF) along the Y-axis.
A: Capacitance measured in voltage-clamp using the Clampex Membrane test severely underestimates Cm. There is a mean difference of 30,5 pF between Control VC (A) and Control CC (B) and 36,2 pF between AcanKO VC (A) and AcanKO CC (B) (n = 13 p<0.0001, paired t-test)
B: AcanKO mice exhibit significantly elevated Cm when compared to control mice; from 55,06 pF in controls to 67,29 pF in AcanKO mice (difference: 12.2 ±4.9 pF, p < 0.05, unpaired t-test)
*(ns = not significant, * = p < 0.05, ** = p < 0.01, *** = p < 0.001)*

3.2 Maximum firing frequency

The maximum firing frequency was tested using the current clamp protocol injecting 1000ms square current steps with increasing intensity, from -350pA to 1100pA in 50pA increments (**Figure 2.3**). The maximum firing frequency was measured during the 1100pA current step as seen in the f-I curve (**Figure 3.5**) and the top sweeps in **Figure 3.4**. At this step, there was no significant difference in maximum firing frequency (462 $\pm$ 54 Hz in controls vs 430 $\pm$ 42 Hz in AcanKO, p = 0.799, Kolmogorov-Smirnov test). There was also no difference in rheobase, and both groups fired the first spikes around 200 pA as seen in the middle sweeps in **Figure 3.4**. Also seen in **Figure 3.4** and **3.5**, neither of the two groups show any sign of adaptation in response to prolonged and increasing stimuli.
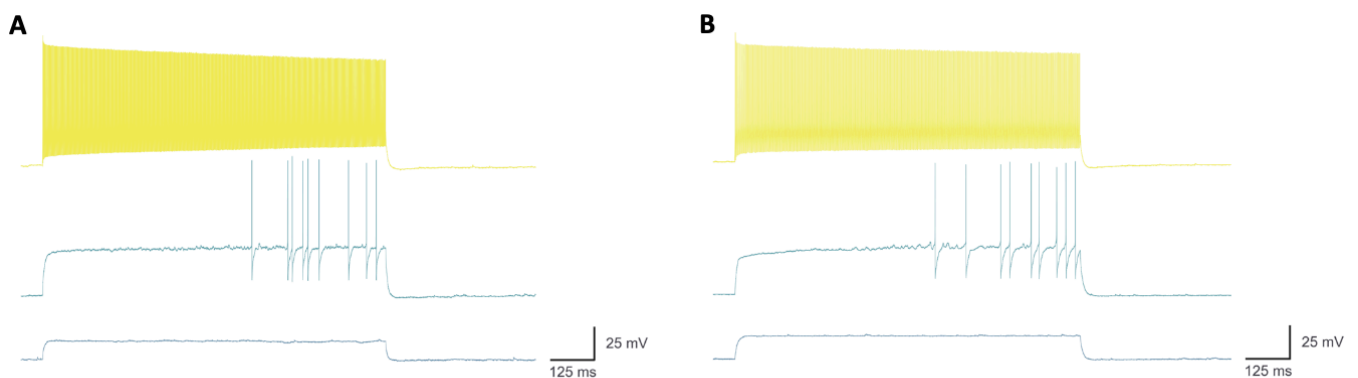
Figure 3.4: Unaltered firing phenotype in controls (A) versus AcanKO mice (B)
A: Last sub-threshold current step (bottom trace), first above-threshold current step (middle trace) and the last current step with maximum firing rate (top trace) in control mice
B: No difference in firing pattern or frequency in the AcanKO mice compared with control mice
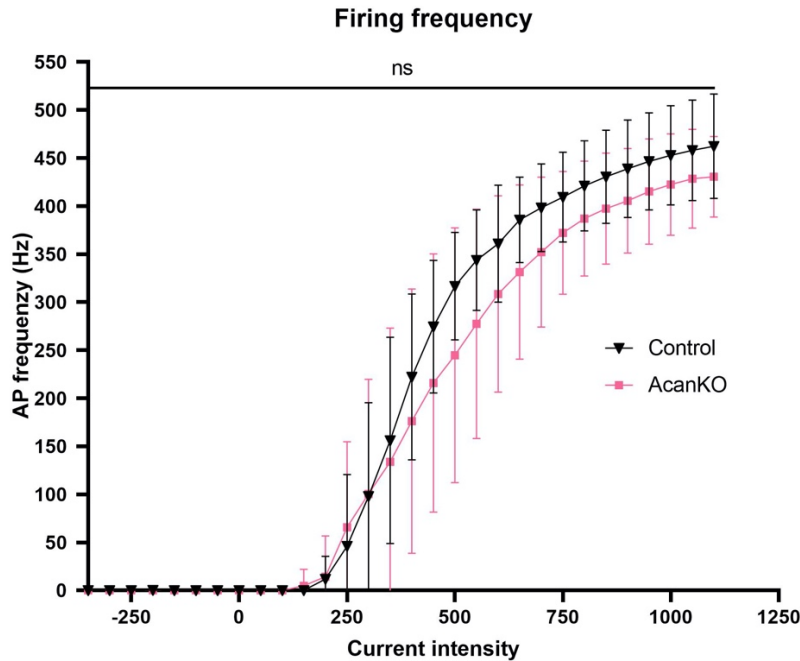
Firing frequency

Figure 3.5: f-I curve comparing firing rate in response to increasing current steps in AcanKO (red) versus control cells (black)
The X-axis represents the current steps in figure 2.3 increasing from -350 pA to 1100 pA. The Y-axis shows the firing frequency in hertz (Hz). No difference in maximum firing rate between control (black) and AcanKO mice (red) (p = 0.799 Kolmogorov-Smirnov test)
*(ns = not significant, * = p < 0.05, ** = p < 0.01, *** = p < 0.001)*

3.3 Spontaneous excitatory postsynaptic currents

In the voltage-clamp protocol, spontaneous excitatory postsynaptic currents (sEPSCs) were recorded continuously for three minutes at -70 mV. Only recordings from the same cells that fulfilled the predetermined quality criteria for the current clamp analyses were included in the voltage-clamp analysis. Two of the control cells from the current-clamp analyses were not recorded in voltage-clamp, and the voltage-clamp analysis is therefore based on 11 cells from control mice, and 13 cells from AcanKO mice. Using unpaired t-tests in Prism 8 (GraphPad Software) to compare controls and AcanKOs, no difference in sEPSCs was found in the AcanKO mice when compared to the controls (**Figure 3.6** & **3.7**). The sEPSC count, mean amp and frequency are all identical in the two groups (Figure 3.6).
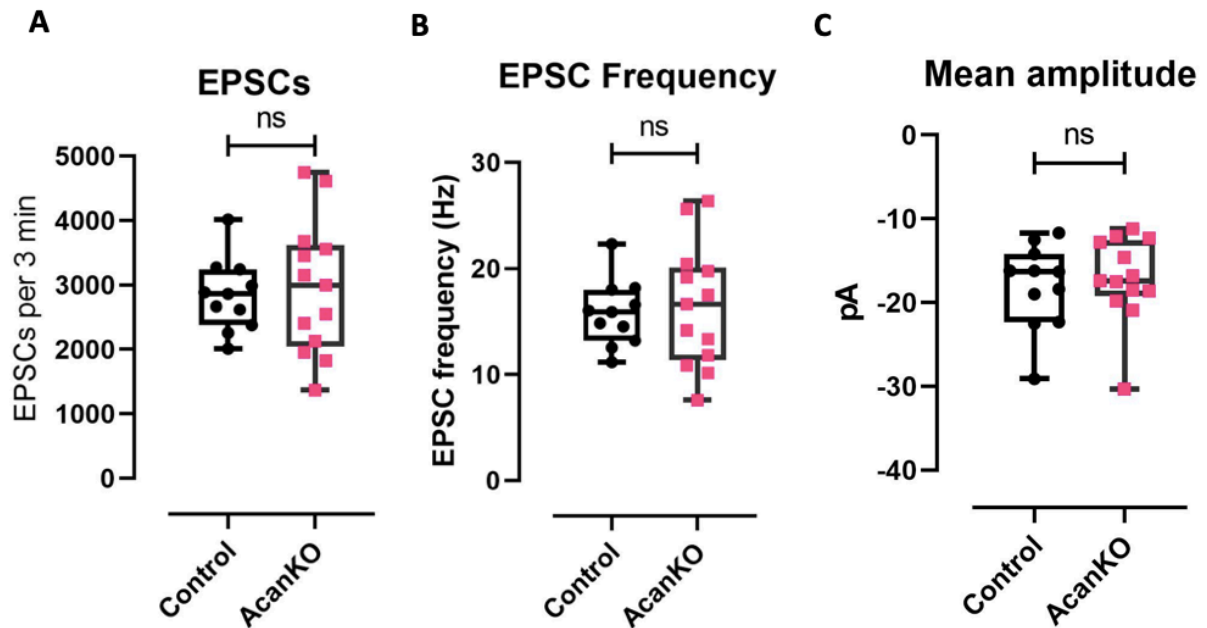
Figure 3.6 Properties of sEPSCs measured in AcanKO cells (red) compared to controls (black)
A: The AcanKO mice had an average of 2956 sEPSCs over 3 min, compared to 2836 in the controls (p = 0.7349, unpaired t-test)
B: The sEPSC frequency is also unchanged (15.75 Hz in controls versus 16.42 Hz in AcanKO, p = 0,73447, unpaired t-test)
C: The sEPSC amplitude remains unaltered as well (-18.04 pA in controls versus -17.14 in AcanKO, p = 0.6696, unpaired t-test)
(ns = not significant, * = p < 0.05, ** = p < 0.01, *** = p < 0.001)

Figure 3.7: *EPSC recordings from control (top) and AcanKO (bottom)*
1-minute cut-outs of the 3-minute recordings show no differences between the control and AcanKO (p = ~0,7, unpaired t-test)

31

4 Discussion

4.1 Methodological considerations

4.1.1 Whole-cell patch-clamping

Whole-cell patch-clamping is a specific and precise way of directly measuring electrical cellular properties in single neurons. Maintaining a tight electrical seal with the pipette in whole-cell mode yields direct, and practically uninterrupted access to the electrical circuits of each cell (Carter and Shieh, 2015). Consequently, the electrical measurements are much more stable and precise than those obtained by extracellular or sharp intracellular electrodes (Li et al., 2004). Furthermore, insight in passive electrical properties such as resting membrane potential, membrane capacitance, input resistance and time constant can be directly measured. Additionally, direct contact between the pipette solution and the intracellular solution opens up the possibility of selectively marking the patched cell with a fluorescent dye, or manipulate the intracellular solution with drugs or by adding or removing essential substances from the intracellular solution(Carter and Shieh, 2015).

Although patch-clamping is excellent for precise measurements of electrical properties in single neurons, whole-cell patch clamp is an invasive technique. With the use of acute brain slices to do recordings, the mice have to be sacrificed immediately before slicing the brain into thinner sections. The slicing is bound to cut a lot of cellular processes and thereby disrupt parts of the cellular network. Furthermore, the pipette must penetrate into the brain slice with applied positive pressure. To the best of my knowledge, only Tewari et al. (2018) have studied the effects of the introduction of a pipette tip onto the cell covered by PNN. They found no pronounced effects on PNN structure after recording in whole-cell mode. Although no effect was seen in that study, *post mortem* fluorescence imaging should be routinely performed after recording to inspect the cell and PNN structure and integrity. Confocal fluorescent imaging was planned, but not feasible for this study (see 6.4 Planned experiments). Although not included here, it will be readily achievable when the microscope becomes available after the SARS-Cov-2 pandemic. Fluorescent imaging will include additional steps of tissue fixation and immunostaining (see 6.4 Planned experiments).

Still another drawback of using the whole-cell configuration is the introduction of an artificial intracellular fluid (Carter and Shieh, 2015). Although adapted to be as similar in contents as possible, artificial intracellular solutions will never have the exact composition as in the intracellular compartments. With each cell being held in the whole-cell mode for about 20 minutes, most of the intracellular solution will be washed out and replaced by the pipette solution. Although necessary to visualize the patched cell to confirm complete reseal after retracting the pipette, several factors that are present in the intracellular solution, but lacking in the pipette solution will also be washed out in the process. Over time, this wash out can potentially affect the recordings. Additionally, liquid junction potentials arise when two different solutions are in contact with each other, adding to the recorded potentials. Liquid

junction potentials have not been corrected for in the present study. Moreover, the oxygen supply is limited by the superfusion of oxygenated recording aCSF when the brain slices are held in the patching chamber. To keep the cells alive for as long as possible, the temperature in the recording chamber must be kept at maximum 31-33°C to reduce metabolism and thereby lowering the need for oxygen. This temperature change may also affect the recordings, although there is only a 4-6°C reduction from the physiological temperature of 37°C.

4.1.2 Subject selection

In a study performed by Lensjo et al. (2017), they show a gradual formation of PNNs from P12 to P21. At P35 or younger, a time interval where several papers have been recording (Carstens et al., 2016; Hayani et al., 2018), Lensjo et al. (2017) showed that the PNNs are only just developed. Albeit completely formed at P30, a structural maturation of PNNs continues until at least P90 (Sigal et al., 2019). To increase the significance of the recordings performed in this study, all recordings were done in adult animals (>P120, average P122 in controls and P149 in AcanKO respectively) where PNNs and neuronal circuits are fully matured. This was achieved by utilizing new NMDG protective brain slicing protocols by Ting et al. (2018). The use of NMDG-substituted aCSF for perfusion, slicing and initial recovery keeps the cells from swelling by osmotic pressure, mostly by reducing the permeability of sodium channel pores, thereby slowing metabolism and reducing stress. Furthermore, the 25 min sodium spike-in gives a gradual transition from low to high sodium concentration in the holding aCSF.

PV^{Cre} c57bl6 mice (B6;129P2-Pvalb$^{tm1(cre)Arbr/J}$ from Jackson Laboratories) were used as controls, as these have normal development of PNNs, but can be injected with one of the two described viruses ([2.2 virus production](#)) to fluorescently label all PV$^+$ cells in the brain. The PV^{Cre} mice are also crossed with Acan-lox mice to produce AcanKO mice as off-spring (Rowlands et al., 2018). To test how the lack of PNNs affect cellular electrophysiology, aggrecan knockout mice (B6(Cg)-ACAN$^{tm1c(EUCOMM)Hmgu>/Jwfa}$) (Rowlands et al., 2018) lacking the protein aggrecan in neural tissue were used. Lacking the essential PNN component aggrecan specifically in the CNS from birth, these mice do not develop PNNs (Rowlands et al., 2018). According to Sykova et al. (2005), KO mice deficient in Tn-R (another PNN component) show structural changes in the extracellular space (ECS). The mice used in that study were Tn-R deficient from birth, and according to Brakebusch et al. (2002) they found a compensatory upregulation of neurocan in mice that were deficient of the PNN lectican brevican from birth. Similarly, aggrecan knockout mice may have developed other mechanisms to compensate for the lack of aggrecan and PNNs, although no such mechanisms are known. Rowlands et al. (2018) also showed that AcanKO mice that do not develop PNNs shift the expression of parvalbumin to a high-plasticity state. Furthermore, Sugiyama et al. (2008) have found that non-cell-autonomous Otx2 is a critical factor in the maturation of the inhibitory PV-cell network, especially in the primary visual cortex, promoting the expression of several PV-specific cell-markers. Among the most important of these markers is the Kv3.1b subunit of

potassium channels, enabling fast-spiking activity in PV$^+$ neurons. PNNs have been shown to enable the specific uptake of Otx2 in PV-cells (Beurdeley et al., 2012; Takesian and Hensch, 2013), and thereby promote late PV-cell maturation and development of fast-spiking activity during the critical period. Strengthening this hypothesis, it has been found that PNN degradation in the adult cortex reduces the number of Otx2 positive cells by 80% (Takesian and Hensch, 2013), indicating a connection between development of PNNs and normal PV-cell maturation. Using AcanKO mice that never develop PNNs might therefore have a bias towards a more immature PV-state, possibly affecting the biophysical cellular properties recorded here. To avoid such potential biases other methods of PNN removal are sought for. One way to go may therefore be the use of acute KO using CRISPR Cas viruses that are cell-type specific. This approach could not be included in the current study, but is highly encouraged for future studies. These, and others are further discussed in 4.4 Future perspectives.

By selectively marking PV$^+$ cells using fluorescent proteins, target specificity for whole-cell recordings was significantly increased. In addition to expressing parvalbumin and being fluorescent, the recorded cells also had to fulfill a set of criteria described in 3 Results. Since only ~ 3 out of 10 cells fulfilled all the predetermined criteria, it may be arguable that the criteria were too strict, excluding potential results. With the aims of this study however, it was more important to ensure high quality of the data than to include all the recorded cells. During my training in patch-clamping and establishment of fluorescent PV-marking, we found empirically that a minority of PV$^+$ cells exhibit maximum firing rates slower than 300 Hz. The cells that were not included were discarded on the basis of one or more of the criteria, for example showing signs of cellular stress, baseline hyperpolarizations and/or unstable capacitance or input resistance.

Further, in this study, all PV$^+$ cells were regarded as one group of fast-spiking cells, although this may be an overly simplified assumption. Several papers (Helm et al., 2013; Rossier et al., 2015; Scala et al., 2020) have shown that there are indeed several subgroups of fast-spiking PV$^+$ interneurons that display differences in cellular electrophysiology. The two main morphoelectrical groups of PV$^+$ neurons are chandelier cells and basket cells. The distinction of PV$^+$ cell subpopulations was, however, beyond the scope of the current study, which has focused on electrophysiological differences in mice that are WT or knockouts for the PNN component aggrecan. To be even more precise, it might have been more elegant to restrict the cellular targets even more, for example only recording from basket cells in layer 4-5 of the primary visual cortex. Although different subgroups of PV-family interneurons are found in different cellular layers and can have different maximum firing frequencies, all fast-spiking neurons are considered electrophysiologically homogenous (Scala et al., 2020). However, it may be useful to take the PV$^+$ subgroups into account when looking at the results of the current study.

4.2 PNNs in neurological disorders

Over the recent years, abnormalities in PNNs and other ECM have been implicated in the pathophysiology of several psychiatric disorders – including schizophrenia, Alzheimer´s and epilepsy (Pantazopoulos and Berretta, 2016). Schizophrenia is characterized by severe psychotic traits and abnormalities in normal emotion and behavior, and it is the neurological disorder in which PNN discrepancies are studied the most. Previously presumed to be a purely neurological disorder, more recent findings suggest that ECM, and particularly PNNs represent a bigger part of the pathophysiology in schizophrenia (Pantazopoulos and Berretta, 2016). *Post mortem* slices of patients with severe schizophrenia show significantly reduced number of *WFA*-positive PNNs in both the amygdala and entorhinal cortex (Pantazopoulos and Berretta, 2016), as well as reduced PV- and PNN-positive cells in the medial prefrontal cortex (Berretta et al., 2015; Testa et al., 2019). Importantly, the decrease in PNN density is not accompanied by cell loss, indicating that PNNs actually take part in the disease progress (Testa et al., 2019). Furthermore, PNNs are not affected in brain areas that are not directly involved in the diseases, such as the primary visual cortex (Pantazopoulos and Berretta, 2016). Genetic analyses have also revealed that some genes are particularly associated with schizophrenia, including PNN components such as Ctrl1 and neurocan, as well as the ECM remodeling enzyme families ADAMTSs and matrix metalloproteinases (MMPs) (Testa et al., 2019). As reviewed by Berretta et al. (2015), studies generally imply that abnormalities in PNNs have profound effects on plasticity and processing of emotions.

Reductions in PNNs in the frontal cortex, without reductions of PV^+ cells, have also been implicated in Alzheimer´s disease (Pantazopoulos and Berretta, 2016). The connection between ECM, PNNs and Alzheimer´s is, however, still enigmatic. β-amyloid plaques, characteristic of the pathophysiology, readily associates with GAG-chains of heparan sulphate proteoglycans similar to CSPGs, while brain areas rich in PNNs containing CSPGs are free from tau-fibrils (Testa et al., 2019). The current results therefore speak to a contradictory role for PNNs in Alzheimer´s disease.

Moreover, PNNs have been implicated in epilepsy as well, although their specific roles are not known. Epilepsy is, however, characterized by an imbalance in neuronal activity, commonly caused by excessive excitatory drive. One of the key functions of PNNs during development is to provide synaptic stability, maturation of PV^+ cells and thereby contribute to establishing adequate inhibitory drive to the E-I balance (Berardi et al., 2004; Takesian and Hensch, 2013). Following seizures, ECM is remodeled by altered expression of MMPs and ECM components, and this remodeling also decreases the number of PNNs (Pantazopoulos and Berretta, 2016). Decreases of PNNs are also associated with reduced threshold for induction of seizures. Tewari et al. (2018) have also found a link between the tumoral release of MMPs and other ECM remodeling enzymes and tumor-associated epileptic seizures. The findings reviewed in this paragraph altogether support a role for ECM and PNNs in neurological and psychiatric

disorders, although it remains elusive if the ECM abnormalities are the cause or consequence of the disorders.

Although PNNs have been implicated in these, and other neurological disorders, the results in this field are still inconclusive (Pantazopoulos and Berretta, 2016), and more targeted research is needed. This study has targeted biophysical properties of PV⁺ interneurons in the primary visual cortex to dissect the functions of PNNs on cellular properties with the hope of clarifying some of the functions of PNNs.

4.3 Measurements of cellular properties

4.3.1 Membrane capacitance

This study has included, and shown results of two ways of measuring Cm, although the current-clamp step (CC-step) calculation protocol is considered the most accurate one (Golowasch et al., 2009). The voltage-clamp step (VC-step) measurement, included in the Clampex membrane test function, grossly underestimates the total membrane capacitance (**Figure 3.3**). Comparing the results of the two different methods for measuring Cm in a paired t-test, a mean difference of 30.5 ± 11.4 pF (n = 13, p < 0.0001) was found between the VC and CC measurements of the control mice. For the AcanKO mice, the difference was 36.2 ± 9.5 pF (n = 13, p < 0.0001). Despite the gross numerical underestimation of Cm with the VC-step method, the relative difference between controls and AcanKO seem to be the same in both VC and CC. The numerical differences in membrane capacitance do, however, strongly encourage the use of current-clamp steps, rather than voltage-clamp measurements as the preferred method of estimating total membrane capacitance.

It has been hypothesized that PNNs capture positive ions in the ECS, and thereby functionally increase the distance between intra- and extracellular media leading to decreased capacitance (Hartig et al., 1999; Morawski et al., 2015). The AcanKO mice used in this study were deficient of the essential PNN component aggrecan from birth. The current study reports a significant increase in membrane capacitance in mice deficient of aggrecan, compared to control mice (**Figure 3.3**). Comparing the most accurate current-clamp calculations in an unpaired t-test, an increase of 12.2 ± 4.9 pF (p<0.05) was found in the AcanKO mice. Although not adding anything to the discussion of ion buffering, the current study has provided results supporting the hypothesis that PNNs decrease Cm. With the function of capacitors in mind, it would be natural to think that an increased capacitance would lead to a decrease in the propagation speed of intracellular electrical signals. Decreasing the speed of intracellular signals should again decrease the maximum frequency of action potentials.

4.3.2 Maximum firing frequency

Together with a decrease in maximum firing rate in AcanKO mice, an increased Cm would support a role for PNNs in facilitating high frequency firing in parvalbumin-expressing interneurons. However, there is no difference in firing frequency (462 ± 54 Hz in controls vs

430 ± 42 Hz in AcanKO, p = 0.799, Kolmogorov-Smirnov test). All cells, both control and AcanKO, follow the same continuous f-I curve with approximately the same maximum frequency (**Figure 3.5**). By recording maximum firing rate in AcanKO mice, no difference was found, and it seems that it is not PNNs, nor a decreased Cm *per se*, that enables the PV^{+} FS neurons to fire at such high rates. To put this in a more physiological perspective, the recorded cells could have been stimulated with a Gaussian white noise protocol (Balmer, 2016; Mainen and Sejnowski, 1995) in addition to the increasing current step protocol. It has been found that although FS basket cells can fire at several hundreds of Hz when stimulated by square step currents, their firing is much more controlled *in vivo*, firing at frequencies below 100 Hz (Kubota, 2014). Balmer (2016) also found that PNN-deficient neurons showing reduced firing frequency when stimulated by the white noise protocol could achieve the same firing frequency as the controls when stimulated by square step currents. It has been argued that the white noise current-clamp protocol represents a more physiological stimuli mimicking synaptic inputs (Mainen and Sejnowski, 1995). This protocol might therefore be better suited to measure the physiological maximum firing frequency of the PV^{+} FS neurons than the steadily increasing current step protocol. It is, however, debatable whether or not it is actually more physiologically relevant. This is because it is a "frozen" white noise protocol, meaning that the white noise is only randomized once, and all the cells are recorded using the exact same white noise. Mathematically speaking, this is in fact not considered noisy, but deterministic.

The lack of differences in maximum firing rate in the present study is, however, clearly different from results published by Tewari et al. (2018) and Balmer (2016), both of which using enzymatic degradation. This indicates that there might be compensatory mechanisms in AcanKO mice that compensates for the loss of PNNs in terms of electrophysiology, or that the chABC treatment affects firing frequency regardless of PNN state. These results therefore increase the need for methodological comparison to unravel the true effects of PNNs and chABC on the electrophysiology of fast-spiking PV-cells.

4.3.3 Spontaneous excitatory postsynaptic currents
Measuring sEPSCs in PV[+] interneurons is a relative measure of the excitatory drive into the PV-network. Excitation of inhibitory PV^{+} cells will result in inhibition of the postsynaptic target cells. The high frequency firing of PV^{+} cells has been implicated in synchronized network firing and establishment of adequate inhibition to the excitation-inhibition balance (Bozzelli et al., 2018; Takesian and Hensch, 2013). It has been proposed that disruptions in PNNs may affect the excitatory input into PV^{+} cells, and thus affect network activity and overall excitatory drive (Bozzelli et al., 2018). In line with this, Lensjø et al. (2017) found that PNN removal resulted in increased disinhibition and increased gamma activity in the hippocampus, while Favuzzi et al. (2017) found reduced excitatory input and inhibitory output from PV^{+} cells in brevican knockout mice. Further implications of this, was that brevican is essential for maturation of glutamatergic input, making PV^{+} cells expressing membrane-bound brevican more efficient in

response to excitatory input than their brevican-deficient counterparts (Favuzzi et al., 2017). Moreover, brevican-deficient mice were found to have cognitive deficits as well, suggesting a role for PNN in establishing balanced and functional network activity in the hippocampus (Favuzzi et al., 2017). The findings regarding EPSCs are in contrast to the results of the present study, in which there was no difference in sEPSCs between control mice and AcanKO mice (**Figure 3.6** & **Figure 3.7**). When comparing with (Favuzzi et al., 2017), the different outcome of electrophysiology in PNN-deficient PV-cells may imply one of two things. Either that the visual cortex compensates for lacking PNNs while the hippocampus does not, or that aggrecan-positive PNNs have different roles than brevican-positive PNNs. Comparing with Lensjø et al. (2017), however, the only difference seems to be the acute degradation by chABC treatment compared to PNN-deficiency from birth. Different results may therefore indicate that it might be the chABC treatment itself, rather than the removal of PNNs that change the electrophysiology of the PV-cells. It is, however, worth mentioning that Lensjø et al. (2017) measured disinhibition and gamma activity using extracellular recordings in rats. Thus, the results presented here further highlights chABC as a potential caveat that should be investigated closely in methodological comparisons.

4.4 Future perspectives

From this, and several other studies (Balmer, 2016; Chu et al., 2018; Faini et al., 2018; Favuzzi et al., 2017; Hayani et al., 2018; Tewari et al., 2018), it is clear that PNN removal affects the electrophysiology of GABAergic PV$^+$ interneurons. Different studies have reported changes in different cellular properties, and with varying significance. The results of the present study were based on only 13 control cells (11 in voltage-clamp), and 13 cells from AcanKO mice. With small test groups and relatively large within-group variation, the results reported here are not as conclusive as they might have been with larger groups. Increasing the population sizes of recorded neurons, would hopefully clarify which cellular properties are actually altered by the PNN removal, and also add to the power of the results.

Further improvements to the experimental design, would be to compare the different methods by which PNNs are removed. In this study, the nets were not actually removed, but the recordings of neurons lacking PNNs were done in mice in which the nets were never developed. Other studies have used the bacterial enzyme chondroitinaseABC to remove the nets. Although shown to effectively disrupt PNNs, chABC has also been shown to affect other ECM structures (Bruckner et al., 1998; Deepa et al., 2006; Tester et al., 2007) which might have contributed to the results of the chABC studies. An interesting approach would be to test the chondroitinase treatment in both control and AcanKO mice, similar to a Tn-R KO/chABC study by Bukalo et al. (2001), creating four different recording groups. This methodological comparison of AcanKO versus chABC treatment was originally included in the aims of this study, and the chABC experiments were prepared and planned to be completed during March/April 2020 (see Appendix 6.4). However, because of the SARS-Cov-2 pandemic, all laboratory access was denied, and I was thereby prevented from performing the chABC

experiments. Although readily accomplishable after the pandemic, the limited time window of a master´s thesis does not allow the wait. Implementing chondroitinase treatment in the current experimental design would allow comparison of the chondroitinase treatment versus the AcanKO, and in addition, evaluate if the chABC enzyme *per se* introduces changes in electrophysiology. Additional experimental comparison could be implicated by testing different administration of the chABC treatment, comparing *in vivo* microinjection directly into the primary visual cortex against acute *post mortem* treatment of slices in both WT and AcanKO mice. The chABC treatment in AcanKO mice would be especially interesting, as previous studies using chABC have reported decreased firing rate and excitatory input (Balmer, 2016; Favuzzi et al., 2017; Tewari et al., 2018), where our AcanKO study found no difference.

To complete the comparison of experimental designs regarding PNN removal, it would be favorable to include a genetic knockout in mice with developed PNNs. This could be implemented by using acute knockout by CRISPR-Cas9, CRISPR-Rx or similar method, specifically targeting essential PNN components in PV[+] interneurons. It could also be done using the Cre-lox system as done by Rowlands et al. (2018). Comparing the cellular electrophysiology of neurons in AcanKOs from birth and viral knockouts could potentially reveal if there are possible biases or compensations in mice that are deficient of PNNs from birth. Looking at the longevity of some EMC proteins, such as collagen and elastin (Toyama and Hetzer, 2013), it was previously been proposed that aggregated PNN components may be equally long-lived with slow turnover (Tsien, 2013), abolishing the phenotypic effect of acute gene knockout. It seems, however, that a profound protein depletion can be attainable within weeks after viral injection (Rowlands et al., 2018), and slow turnover should consequently not be a big issue.

Still another possibility to target fully developed PNNs *in vivo*, could be to genetically upregulate the expression of matrix degrading enzymes. Both proteases of the ADAMTS and MMP families are good candidates for this, as they have been shown to target aggrecan as well as other ECM components (Tewari et al., 2018). This can be done in several ways, and I will not go into detail about these. Tewari et al. (2018) have used a tumoral mouse model expressing increased levels of MMPs and ADAMTSs when studying PV^{+} cells in an epilepsy study. An advantage of regulating the matrix degrading enzymes is that it may represent a more physiologically relevant experiment, because it exploits a regulation system that already exist in normal mice. Conversely, a disadvantage is that it is unrealistic to achieve specific and total degradation of PNNs without degrading much of the loose ECM as well, making it more difficult to draw clear conclusions from the results. I will not go into detail about the options on regulating existing systems, but I mention them to underline the extensive list of possibilities.

Lastly, to exploit more of the potential of whole-cell patch-clamping, it would be preferable to include post-recording 3D-reconstruction of the recorded cells. This was also originally planned, but was unfortunately not achievable within the frames of this thesis due to the closed laboratories during the SARS-Cov-2 pandemic. Staining and imaging the recorded neurons would further increase the power of the results by conforming specificity of PV cells in the primary visual cortex, and ensure that the recorded cells are intact. Importantly, 3D-reconstruction also allows for evaluation of the PNN-status, to confirm that all control cells have well-developed PNNs, and that the knockouts/enzyme treated cells do not. Adding post-recording reconstruction would thereby add another layer of confidence to the experimental design, by confirming that the experiment is actually hitting the desired target, and with greater certainty measuring the effects of PNN removal.

4.5 Concluding remarks

The focus of this study was to dissect how perineuronal nets influence the electrophysiology of parvalbumin-expressing interneurons in the primary visual cortex. To achieve this, whole-cell patch-clamp recordings of PV+ cells in the primary visual cortex of AcanKO mice deficient of PNNs from birth were compared to recordings from control mice. The results of these recordings show that AcanKO mice exhibit significantly increased membrane capacitance compared to controls, but no differences in the other electrophysiologic properties investigated. These results thereby add to the conflicting results in the literature, but also indicate that AcanKO mice somehow compensates for not having PNNs when comparing with the results of other means of removing PNNs.

This study also intended to compare the electrophysiology of AcanKO and control mice to mice treated with the bacterial enzyme chondroitinaseABC as a comparative control experiment. These experiments were unfortunately hindered by the SARS-Cov-2 pandemic, and are not included. The need for methodological comparison and future advances is still highlighted by this thesis, pointing out a path for future experiments.

5 References

Atasoy, D., et al., 2008. A FLEX switch targets Channelrhodopsin-2 to multiple cell types for imaging and long-range circuit mapping. J Neurosci. 28**,** 7025-30.

Balmer, T.S., 2016. Perineuronal Nets Enhance the Excitability of Fast-Spiking Neurons. Eneuro. 3.

Bekkers, J.M., 2011. Pyramidal neurons. Current Biology. 21**,** R975.

Berardi, N., Pizzorusso, T., Maffei, L., 2004. Extracellular matrix and visual cortical plasticity: freeing the synapse. Neuron. 44**,** 905-8.

Berretta, S., et al., 2015. Losing the sugar coating: potential impact of perineuronal net abnormalities on interneurons in schizophrenia. Schizophr Res. 167**,** 18-27.

Beurdeley, M., et al., 2012. Otx2 binding to perineuronal nets persistently regulates plasticity in the mature visual cortex. J Neurosci. 32**,** 9429-37.

Bozzelli, P.L., et al., 2018. Proteolytic Remodeling of Perineuronal Nets: Effects on Synaptic Plasticity and Neuronal Population Dynamics. Neural Plast. 2018**,** 5735789.

Brakebusch, C., et al., 2002. Brevican-deficient mice display impaired hippocampal CA1 long-term potentiation but show no obvious deficits in learning and memory. Mol Cell Biol. 22**,** 7417-27.

Bruckner, G., et al., 1998. Acute and long-lasting changes in extracellular-matrix chondroitin-sulphate proteoglycans induced by injection of chondroitinase ABC in the adult rat brain. Exp Brain Res. 121**,** 300-10.

Bukalo, O., Schachner, M., Dityatev, A., 2001. Modification of extracellular matrix by enzymatic removal of chondroitin sulfate and by lack of Tenascin-R differentially affects several forms of synaptic plasticity in the hippocampus. Neuroscience. 104**,** 359-369.

Carstens, K.E., et al., 2016. Perineuronal Nets Suppress Plasticity of Excitatory Synapses on CA2 Pyramidal Neurons. J Neurosci. 36**,** 6312-20.

Carter, M., Shieh, J., 2015. Guide to Research Techniques in Neuroscience, Vol. 2, Academic Press.

Carulli, D., et al., 2006. Composition of perineuronal nets in the adult rat cerebellum and the cellular origin of their components. J Comp Neurol. 494**,** 559-77.

Carulli, D., et al., 2010. Animals lacking link protein have attenuated perineuronal nets and persistent plasticity. Brain. 133**,** 2331-47.

Celio, M.R., Blumcke, I., 1994. Perineuronal nets--a specialized form of extracellular matrix in the adult nervous system. Brain Res Brain Res Rev. 19**,** 128-45.

Challis, R.C., et al., 2019. Systemic AAV vectors for widespread and targeted gene delivery in rodents. Nature Protocols. 14**,** 379-414.

Chan, K.Y., et al., 2017. Engineered AAVs for efficient noninvasive gene delivery to the central and peripheral nervous systems. Nat Neurosci. 20**,** 1172-1179.

Chu, P., et al., 2018. The Impact of Perineuronal Net Digestion Using Chondroitinase ABC on the Intrinsic Physiology of Cortical Neurons. Neuroscience. 388**,** 23-35.

Connors, B.W., Gutnick, M.J., 1990. Intrinsic firing patterns of diverse neocortical neurons. Trends in Neurosciences. 13**,** 99-104.

Deepa, S.S., et al., 2006. Composition of perineuronal net extracellular matrix in rat brain: a different disaccharide composition for the net-associated proteoglycans. J Biol Chem. 281**,** 17789-800.

Deyle, D.R., Russell, D.W., 2009. Adeno-associated virus vector integration. Curr Opin Mol Ther. 11**,** 442-7.

Dityatev, A., et al., 2007. Activity-dependent formation and functions of chondroitin sulfate-rich extracellular matrix of perineuronal nets. Dev Neurobiol. 67**,** 570-88.

Faini, G., et al., 2018. Perineuronal nets control visual input via thalamic recruitment of cortical PV interneurons. Elife. 7.

Favuzzi, E., et al., 2017. Activity-Dependent Gating of Parvalbumin Interneuron Function by the Perineuronal Net Protein Brevican. Neuron. 95**,** 639-655 e10.

Fawcett, J.W., Oohashi, T., Pizzorusso, T., 2019. The roles of perineuronal nets and the perinodal extracellular matrix in neuronal function. Nature Reviews Neuroscience. 20**,** 451-465.

Galtrey, C.M., Fawcett, J.W., 2007. The role of chondroitin sulfate proteoglycans in regeneration and plasticity in the central nervous system. Brain Res Rev. 54**,** 1-18.

Gentet, L.J., Stuart, G.J., Clements, J.D., 2000. Direct measurement of specific membrane capacitance in neurons. Biophys J. 79**,** 314-20.

Golowasch, J., et al., 2009. Membrane capacitance measurements revisited: dependence of capacitance value on measurement method in nonisopotential neurons. J Neurophysiol. 102, 2161-75.

Gottschling, C., et al., 2019. Elimination of the four extracellular matrix molecules tenascin-C, tenascin-R, brevican and neurocan alters the ratio of excitatory and inhibitory synapses. Sci Rep. 9, 13939.

Hamai, A., et al., 1997. Two distinct chondroitin sulfate ABC lyases. An endoeliminase yielding tetrasaccharides and an exoeliminase preferentially acting on oligosaccharides. J Biol Chem. 272, 9123-30.

Harden, S., 2020. Analysis of electrophysiological recordings was performed with custom software written for this project using Python 3.7 and the pyABF module. Vol. 2020, ed.^eds.

Hartig, W., Brauer, K., Bruckner, G., 1992. Wisteria floribunda agglutinin-labelled nets surround parvalbumin-containing neurons. Neuroreport. 3, 869-72.

Hartig, W., et al., 1999. Cortical neurons immunoreactive for the potassium channel Kv3.1b subunit are predominantly surrounded by perineuronal nets presumed as a buffering system for cations. Brain Res. 842, 15-29.

Hayani, H., Song, I., Dityatev, A., 2018. Increased Excitability and Reduced Excitatory Synaptic Input Into Fast-Spiking CA2 Interneurons After Enzymatic Attenuation of Extracellular Matrix. Frontiers in cellular neuroscience. 12, 149-149.

Helm, J., Akgul, G., Wollmuth, L.P., 2013. Subgroups of parvalbumin-expressing interneurons in layers 2/3 of the visual cortex. J Neurophysiol. 109, 1600-13.

Herculano-Houzel, S., 2014. The glia/neuron ratio: how it varies uniformly across brain structures and species and what that means for brain physiology and evolution. Glia. 62, 1377-91.

Hippenmeyer, S., et al., 2005. A developmental switch in the response of DRG neurons to ETS transcription factor signaling. PLoS Biol. 3, e159.

Hrabetova, S., et al., 2009. Calcium diffusion enhanced after cleavage of negatively charged components of brain extracellular matrix by chondroitinase ABC. J Physiol. 587, 4029-49.

Hu, H., Gan, J., Jonas, P., 2014. Interneurons. Fast-spiking, parvalbumin(+) GABAergic interneurons: from cellular design to microcircuit function. Science. 345, 1255263.

Hu, H., Jonas, P., 2014. A supercritical density of Na(+) channels ensures fast signaling in GABAergic interneuron axons. Nat Neurosci. 17**,** 686-93.

Huang, Z.J., Paul, A., 2019. The diversity of GABAergic neurons and neural communication elements. Nat Rev Neurosci. 20**,** 563-572.

Kandel, E., et al., 2012a. Membrane Potential. In: Principles of Neural Science. Vol. Fifth edition, ed.^eds. Elsevier, pp. 125-139.

Kandel, E., et al., 2012b. Nerve Cells. In: Principles of Neural Science. Vol. Fifth edition, ed.^eds. Elsevier pp. 19-35.

Kawaguchi, Y., Kubota, Y., 1997. GABAergic cell subtypes and their synaptic connections in rat frontal cortex. Cereb Cortex. 7**,** 476-86.

Kubota, Y., 2014. Untangling GABAergic wiring in the cortical microcircuit. Curr Opin Neurobiol. 26**,** 7-14.

Kwok, J.C., et al., 2011. Extracellular matrix and perineuronal nets in CNS repair. Dev Neurobiol. 71**,** 1073-89.

Lee, S., et al., 2010. The largest group of superficial neocortical GABAergic interneurons expresses ionotropic serotonin receptors. J Neurosci. 30**,** 16796-808.

Lensjo, K.K., et al., 2017. Differential Expression and Cell-Type Specificity of Perineuronal Nets in Hippocampus, Medial Entorhinal Cortex, and Visual Cortex Examined in the Rat and Mouse. eNeuro. 4.

Lensjø, K.K., et al., 2017. Removal of Perineuronal Nets Unlocks Juvenile Plasticity Through Network Mechanisms of Decreased Inhibition and Increased Gamma Activity. The Journal of Neuroscience. 37**,** 1269-1283.

Li, W.C., Soffe, S.R., Roberts, A., 2004. A direct comparison of whole cell patch and sharp electrodes by simultaneous recording from single spinal neurons in frog tadpoles. J Neurophysiol. 92**,** 380-6.

Lodato, S., Arlotta, P., 2015. Generating neuronal diversity in the mammalian cerebral cortex. Annu Rev Cell Dev Biol. 31**,** 699-720.

Mainen, Z.F., Sejnowski, T.J., 1995. Reliability of spike timing in neocortical neurons. Science. 268**,** 1503-6.

Molleman, A., 2003. Patch clamping: An Introductory Guide To Patch Clamp Electrophysiology, Vol., John Wiley & Sons.

Morawski, M., et al., 2004. Perineuronal nets potentially protect against oxidative stress. Exp Neurol. 188**,** 309-15.

Morawski, M., et al., 2015. Ion exchanger in the brain: Quantitative analysis of perineuronally fixed anionic binding sites suggests diffusion barriers with ion sorting properties. Sci Rep. 5**,** 16471.

Morris, N.P., Henderson, Z., 2000. Perineuronal nets ensheath fast spiking, parvalbumin-immunoreactive neurons in the medial septum/diagonal band complex. Eur J Neurosci. 12**,** 828-38.

Pantazopoulos, H., Berretta, S., 2016. In Sickness and in Health: Perineuronal Nets and Synaptic Plasticity in Psychiatric Disorders. Neural Plast. 2016**,** 9847696.

Paxinos, G., and Keith B.J. Franklin, 2001. The mouse brain in stereotaxic coordinates: hard cover edition, Vol. 2 edition, Academic Press.

Petilla Interneuron Nomenclature, G., et al., 2008. Petilla terminology: nomenclature of features of GABAergic interneurons of the cerebral cortex. Nat Rev Neurosci. 9**,** 557-68.

Pizzorusso, T., et al., 2002. Reactivation of ocular dominance plasticity in the adult visual cortex. Science. 298**,** 1248-51.

Romberg, C., et al., 2013. Depletion of Perineuronal Nets Enhances Recognition Memory and Long-Term Depression in the Perirhinal Cortex. Journal of Neuroscience. 33**,** 7057-7065.

Rossier, J., et al., 2015. Cortical fast-spiking parvalbumin interneurons enwrapped in the perineuronal net express the metallopeptidases Adamts8, Adamts15 and Neprilysin. Mol Psychiatry. 20**,** 154-61.

Rowlands, D., et al., 2018. Aggrecan Directs Extracellular Matrix-Mediated Neuronal Plasticity. J Neurosci. 38**,** 10102-10113.

Saunders, A., Johnson, C.A., Sabatini, B.L., 2012. Novel recombinant adeno-associated viruses for Cre activated and inactivated transgene expression in neurons. Front Neural Circuits. 6**,** 47.

Scala, F., et al., 2020. Phenotypic variation within and across transcriptomic cell types in mouse motor cortex. bioRxiv. 2020.02.03.929158.

Sigal, Y.M., et al., 2019. Structural maturation of cortical perineuronal nets and their perforating synapses revealed by superresolution imaging. Proc Natl Acad Sci U S A. 116**,** 7071-7076.

Sugiyama, S., et al., 2008. Experience-dependent transfer of Otx2 homeoprotein into the visual cortex activates postnatal plasticity. Cell. 134**,** 508-20.

Sykova, E., et al., 2005. Reduced extracellular space in the brain of tenascin-R- and HNK-1-sulphotransferase deficient mice. Eur J Neurosci. 22**,** 1873-80.

Takesian, A.E., Hensch, T.K., 2013. Balancing Plasticity/Stability Across Brain Development. Changing Brains Applying Brain Plasticity to Advance and Recover Human Ability. 207**,** 3-34.

Testa, D., Prochiantz, A., Di Nardo, A.A., 2019. Perineuronal nets in brain physiology and disease. Semin Cell Dev Biol. 89**,** 125-135.

Tester, N.J., Plaas, A.H., Howland, D.R., 2007. Effect of body temperature on chondroitinase ABC's ability to cleave chondroitin sulfate glycosaminoglycans. J Neurosci Res. 85**,** 1110-8.

Tewari, B.P., et al., 2018. Perineuronal nets decrease membrane capacitance of peritumoral fast spiking interneurons in a model of epilepsy. Nat Commun. 9**,** 4724.

Ting, J.T., et al., 2018. Preparation of Acute Brain Slices Using an Optimized N-Methyl-D-glucamine Protective Recovery Method. Jove-Journal of Visualized Experiments.

Toyama, B.H., Hetzer, M.W., 2013. Protein homeostasis: live long, won't prosper. Nat Rev Mol Cell Biol. 14**,** 55-61.

Tremblay, R., Lee, S., Rudy, B., 2016. GABAergic Interneurons in the Neocortex: From Cellular Properties to Circuits. Neuron. 91**,** 260-92.

Tsien, R.Y., 2013. Very long-term memories may be stored in the pattern of holes in the perineuronal net. Proc Natl Acad Sci U S A. 110**,** 12456-61.

van 't Spijker, H.M., Kwok, J.C.F., 2017. A Sweet Talk: The Molecular Systems of Perineuronal Nets in Controlling Neuronal Communication. Frontiers in Integrative Neuroscience. 11.

Vitellaro-Zuccarello, L., De Biasi, S., Spreafico, R., 1998. One hundred years of Golgi's "perineuronal net": history of a denied structure. Ital J Neurol Sci. 19**,** 249-53.

Wang, D., Fawcett, J., 2012. The perineuronal net and the control of CNS plasticity. Cell Tissue Res. 349**,** 147-60.

Yamaguchi, Y., 2000. Lecticans: organizers of the brain extracellular matrix. Cell Mol Life Sci. 57**,** 276-89.

6 Appendix

6.1 List of abbreviations

5HT3aR	5-hydroxytryptamine 3a receptor (Ionotropic serotonin receptor)
AAV	Adeno-associated virus
AcanKO	aggrecan knockout
aCSF	artificial cerebrospinal fluid
ADAMTS	a disintegrin and metalloproteinase with thrombospondin motifs
AMPA	α-amino-3-hydroxy-5-methyl-4-isoxazolepropionic acid
AP	action potential
ATP	adenosine tri-phosphate
CC	current-clamp
chABC	chondroitinase ABC
Cm	membrane capacitance
CNS	central nervous system
CSPG	chondroitin sulfate proteoglycan
Ctrl1	cartilage linkage protein 1
DIC	differential interference contrast
ECM	extracellular matrix
ECS	extracellular space
EGTA	Ethylene glycol-bis(2-aminoethylether)-N,N,N',N'-tetraacetic acid
f-I curve	frequency-current intensity curve
FS	fast-spiking
GABA	gamma-aminobutyric acid
HA	hyaluronic acid
Hapln1/4	hyaluronan binding protein 1/4
HEPES	4-(2-hydroxyethyl)-1-piperazineethanesulfonic acid
ITR	inverted terminal repeats
MMP	matrix metalloproteinase
mOsm	milli-osmole
NMDG	N-Methyl-D-glucamine

PBS	phosphate-buffered saline
PNN	perineuronal net
PV	parvalbumin
rAAV	recombinant AAV
RMP	resting membrane potential
RS	regular-spiking
sEPSC	spontaneous excitatory postsynaptic current
Sst	somatostatin
Tn-R	tenascin R
VC	voltage-clamp
VIP	vasoactive intestinal peptide
WFA	*Wisteria floribunda* agglutinin

6.2 Solutions used for transcardial perfusion, slice preparation and patching

6.2.1 NMDG-HEPES recovery aCSF:

Table 1: NMDG-HEPES recovery aCSF. Solution recipe from Ting et al. (2018).

Reagent	mM	MW (g/mol)	g/L	g/2L	
NMDG	93	195.2	18.16	36.311	
(HCl)					(10M stock)
KCl	2.5	74.6	0.19	0.373	
NaH_2PO_4	1.2	138.0	0.17	0.3312	
$NaHCO_3$	30	84.0	2.52	5.041	
HEPES	20	238.3	4.77	9.5324	
Glucose	25	180.2	4.51	9.010	
Sodium ascorbate	5	198.0	0.99	1.98	
Thiourea	2	76.1	0.15	0.304	
Sodium pyruvate	3	110.0	0.33	0.66024	
$MgSO_4{\bullet}7H_2O$	10	246.5	5ml	10ml	(2M stock)
$CaCl_2{\bullet}2H_2O$	0.5	147.0	250µl	500µl	(2M stock)

Make 2L and titrate to pH 7.3-7.4 using 10M HCl. Osmolarity should be 300-310 mOsm.

6.2.2 HEPES holding aCSF:

Table 2: HEPES holding aCSF. Solution recipe from Ting et al. (2018).

Reagent	mM	MW (g/mol)	g/L	
NaCl	92	58.4	5.38	
KCl	2.5	74.6	0.19	
NaH_2PO_4	1.2	138.0	0.17	
$NaHCO_3$	30	84.0	2.52	
HEPES	20	238.0	4.77	
Glucose	25	180.2	4.51	
Sodium ascorbate	5	198.0	0.99	
Thiourea	2	76.1	0.15	
Sodium pyruvate	3	110.0	0.33	
$MgSO_4{\bullet}7H_2O$	2	246.5	1ml	(2M stock)
$CaCl_2{\bullet}2H_2O$	2	147.0	1ml	(2M stock)

Osmolarity should be 300-310 mOsm. Make 1L and adjust pH to 7.3-7.4 using NaOH or HCl.

6.2.3 Recording aCSF:

Table 3: Recording aCSF. Solution recipe from Ting et al. (2018).

Reagent	mM	MW (g/mol)	g/L	
NaCl	124	58.4	7.25	
KCl	2.5	74.6	0.19	
NaH_2PO_4	1.2	138.0	0.17	
$NaHCO_3$	24	84.0	2.02	
HEPES	5	238.3	1.19	
Glucose	12.5	180.2	2.25	
$MgSO_4{\bullet}7H_2O$	2	246.5	1ml	(2M stock)
$CaCl_2{\bullet}2H_2O$	2	147.0	1ml	(2M stock)

Make 1L, and titrate to pH 7.3-7.4 using NaOH or HCl if necessary. Osmolarity should be 300-310 mOsm.

6.2.4 Na+ spike-in solution (5 M):

Solution recipe from Ting et al. (2018).
580 mg of NaCl dissolved in 5 ml of freshly prepared, oxygenated NMDG-HEPES aCSF. This is enough for one brain slice preparation.

6.2.5 Intracellular pipette solution

Table 4: Intracellular solution for recording interneurons. Recipe from (Hu and Jonas, 2014)

Reagent	mM	g	
K-gluconate	120	2.811	
KCl	20	2 ml	(1M stock)
EGTA	10	0.3804	
HEPES	10	0.2383	
$MgCl_2$	2	200µl	(1M stock)
Na_2ATP	2	0.1102	

Make 100 ml and adjust pH to 7.3. Osmolarity should be ~300mOsm, or increased to ~mOsm below the recording aCSF osmolarity.

6.3 Specific protocols

6.3.1 Sodium spike-in protocol

To avoid too much disturbance of the slices, the sodium solution was added to the bubbling chimney.

Time in recovery	Amount of 5M sodium solution added
0 min	250 μl
5 min	250 μl
10 min	500 μl
15 min	1000 μl
20 min	2000 μl
25 min	Transfer to HEPES-holding aCSF

6.3 Solutions for tissue fixation and immunohistochemistry

6.3.1 4% Formaldehyde

Mix 10 ml 16% formaldehyde (Thermo Scientific, Rockford, IL, USA) in 30 ml 1X PBS to make 40 ml 4% formaldehyde.

6.3.2 10X PBS

Table 6: 10X PBS

Reagent	MW (g/mol)	g/L
NaCl	58.44	80.0
KCl	74.55	2.00
Na_2HPO_4	141.96	14.4
KH_2PO_4	136.1	2.40

Dissolve in 800 ml dH2O, adjust pH to 7.4 and adjust volume to 1.0L. dilute 1:10 to make 1X PBS.

6.4 Planned experiments

Here, I present the experiments I had planned for the chABC treatment, along with the protocol for post patch immunostaining. These experiments were scheduled to be done in March/April, but could not be performed due to the SARS-Cov-2 pandemic. Due to all the time invested in the careful planning and for completeness of the thesis project I present them here.

6.4.1 *In vivo* chABC injection

To test the effect of chABC treatment on electrophysiology, two different approaches were planned. Firstly, *in vivo* microinjections of chABC were planned to compare enzymatic degradation of the perineuronal nets to the results obtained from the control and AcanKO mice. The microinjections would have been performed approximately one week before recording similarly to what is described by Lensjø et al. (2017), as I will briefly summarize here.

For the local microinjections chondroitinase ABC (C3667, Sigma-Aldrich) from *Proteus vulgaris* would be diluted in filtered 1X PBS to 0.05U/ml (Lensjø et al., 2017; Pizzorusso et al., 2002). To enable precise and reliable injections, the chABC dilution would be loaded in sterile glass pipettes with an opening diameter of about 15 μm, and mounted onto a NanoJect 3.0 microinjector (Drummond Scientific, USA). Volumes and injection rates would be appropriately adjusted according to the size of the mice.

All surgeries were to be performed in a designated surgery room within the animal facility at the IBM, Faculty of Medicine, UoO in an aseptic environment. The mice would be deeply anesthetized using 5% isoflurane mixed with air, checked for hindlimb toe pinch reflexes, and anesthesia would be maintained with 1.5-2% isoflurane through a mouse facial mask. While anesthetized with isoflurane, they would also be immobilized in a stereotaxic frame (Koppf Instruments, USA), before administrating local anesthesia and analgesia subcutaneously. Throughout the whole surgery, body temperature and heart rate would be constantly monitored (Somnosuite, Kent Scientific, USA). While fully anesthetized, the scalp would then have to be shaved and cleaned before making a small cut to access the scull. Centered over the primary visual cortex, with coordinates bregma = -4 and 2.5mm lateral of lambda, craniotomies of approximately 1.5mm would be made using a hand-held Perfecta 300 dental drill (W & H Nordic). The coordinates are based on the mouse brain atlas (Paxinos, 2001). The chABC would then be injected approximately 500μm below the *dura* using a Nanoject 3.0 (USA) injection pump. After injection, the craniotomies would be sealed using KwikSil silicone (World Precision Instruments) and the wound sutured shut. The edges of the wound would further be cleaned and treated with local anesthetics after surgery, and routinely over the next few days. Approximately one week after surgery and chABC injection, these mice would be perfused and acute slices would be prepared and recorded exactly as the control and AcanKO mice, described in 2.3 Patch-clamp experiments.

6.4.2 Acute *post mortem* slice chABC incubation
To add a comparison of *in vivo injection* and acute *post mortem* treatment, slices of both control and AcanKO mice were planned to be incubated in a recovery chamber containing chondroitinase ABC (C3667, Sigma-Aldrich) from *Proteus vulgaris*. These slices would be incubated at 33°C for 45 minutes in a small chamber containing 0.5 U/ml chABC in 2ml HEPES holding buffer under constant oxygenation. Following the 45 min incubation, the chABC treated slices would be recorded exactly as the untreated slices, as described in 2.3.3.

6.4.3 Post-recording histology and imaging
After patching, slices in which the recorded cell seemed intact, were to be fixed in 4% Paraformaldehyde (Thermo Scientific, Rockford, IL, USA) overnight, before being stained with fluorescent antibodies. The slices would be rinsed in a petri dish with 1X phosphate-buffered saline (PBS) before being rinsed 3 x 2 min in 1X PBS in a 24-well plate. Following the rinse in PBS, the brain slices were to be washed 3 x 30 min in ~0.5 ml washing solution (MAXwash™,

Active Motif), before a 2-hour incubation in blocking solution (MAXblock™, Active Motif). All slices would be stained using biotin-conjugated WFA (1:500, Sigma-Aldrich L1516, Germany) as primary staining and AlexaFluor™ streptavidin-647 (1:500, Thermo Fisher Scientific, S32357) as secondary staining in staining solution (MAXbind™, Active Motif). The sections would be washed 3 X 30 min in washing solution between primary and secondary staining, and also after the secondary staining. To achieve robust and reliable WFA staining, both primary and secondary staining would be incubated for approximately 48 hours each.

Following histology, all stained slices would be imaged at the Oslo NorMIC Imaging facility at the IBV, Faculty of Mathematics and Natural sciences, UoO. This imaging platform is equipped with an Andor DragonFly spinning disk confocal microscope with a Zyla4.2 sCMOS 2048x2048 camera. The slices would be imaged with both a 20X, 0.75 N.A. air objective (CFI Plan Apo) and a 60X, 1.2 N.A. water-immersion objective (CFI Plan Apo), making detailed z-stacks for 3D-reconstruction of the patched cells.

Proceeding the SARS-Cov-2 pandemic, the DragonFly microscope was first unavailable for master students and then for longer periods of time due to busy booking schedules and unforeseen technical issues. I was therefore prevented from including the histology and imaging in the analyses and results.